Article

Proteome-wide ligandability maps of drugs with diverse cysteine-reactive chemotypes

Caiping Tian[1,2,6], Lu Sun[3,4,6], Keke Liu[1], Ling Fu[1], Yi Zhang[3], Wendong Chen[5], Fuchu He [1,5] ✉ & Jing Yang [1,3,4,5] ✉

Covalent drug discovery has experienced a revival since the 2013 approval of the first cysteine-targeting kinase inhibitors. Many drugs that were discovered by serendipity also possess the ability to react with cysteine residues, leading to interactions with multiple proteins. This widespread interaction, known as promiscuity, necessitates a comprehensive study of how these drugs engage with cysteines throughout the proteome. Here we report a large-scale analysis to meet this need by defining proteome-wide cysteine ligandability maps of 70 drugs in native biological systems. We examined over 24,000 cysteines in the human proteome, pinpointing 279 proteins as potential drug targets across diverse functional categories. We further validated several cysteine engagement events, uncovering previously unknown cysteine sites on both established drug targets and proteins that are generally difficult to address with small molecules. Additionally, our findings highlighted an opportunity to harness a drug-cysteine interaction for targeted protein degradation. Together, our analysis provides an invaluable resource for advancing the development of covalent drugs.

Covalent drugs, a distinctive class of small molecules, act by forming covalent bonds with amino acids on target proteins. While early examples, such as aspirin, and blockbuster drugs like omeprazole and clopidogrel, have demonstrated the effectiveness of this approach, covalent inhibitors were historically underutilized in drug development due to concerns about off-target effects and toxicity. Over the past decade, however, advances in rational design have shown that covalent drugs can be highly selective, leading to the emergence of targeted covalent inhibitors (TCIs)[1]. TCIs have achieved significant success in addressing key therapeutic targets, such as EGFR and BTK, in cancer treatment. They have also expanded possibilities for targeting "undruggable" proteins, like mutant KRAS[G12C], highlighting the ongoing importance of this drug class.

Most FDA (the US Food and Drug Administration)-approved TCIs utilize acrylamide or its structural variants as electrophilic warheads, enabling covalent modification of cysteine residues when guided by precise molecular recognition. Beyond acrylamides, other cysteine-reactive chemotypes have been identified in certain clinical drugs with demonstrated efficacy and manageable safety profiles. Notably, many of these drugs were discovered serendipitously rather than through deliberate design. Consequently, poly-pharmacology, where drugs interact with multiple targets, is a common feature of these agents. For instance, the immunomodulatory drug dimethyl fumarate covalently modifies various therapeutic targets, including GAPDH[2], GSDMD[3], RSK2[4], IRAK4[5] and PRKCQ[6], via cysteine succination. Despite these advances, our understanding of the interactions between cysteine-reactive drugs and the broader human cysteinome remains limited.

Activity-based protein profiling (ABPP), particularly in a competitive format, has emerged as the method of choice for mapping the proteomic interactions of electrophilic small molecules[7]. This method

evaluates the ability of cysteine-reactive compounds to compete with a thiol-reactive probe[8], enabling the profiling of electrophile-target interactions. Recent studies have significantly expanded our knowledge of cysteine ligandability in human and bacterial proteomes by applying competitive ABPP to libraries of synthetic electrophiles[9–14]. Building on this foundation, we developed the Quantitative Thiol Reactivity Profiling (QTRP) method[15], which has proven effective for deconvoluting the targets of electrophilic natural products in native biological systems[16–19].

In this study, we present a QTRP-based chemoproteomic analysis of 70 drugs, including 58 FDA-approved medicines, screened against over 24,000 human cysteines in vitro and/or *in cellulo*. To our knowledge, this represents the most comprehensive dataset for investigating covalent drug-target interactions. This resource provides a unique opportunity to elucidate previously uncharacterized covalent mechanisms of action, and explore innovative applications such as repurposing an existing drug as the covalent recruiter for targeted protein degradation.

Results

Screening the cysteinome reactivity of drugs with cysteine-reactive chemotypes

To investigate cysteine reactivity across a diverse set of drugs, we compiled a library of small molecules with known or potential cysteine-reactive chemotypes (Supplementary Fig. 1). This library includes 66 pharmaceuticals, 2 nutraceuticals (i.e., cystine, lipoid acid) and 2 pharmaceutical cosmetics (i.e., Octinoxate, Enzacamene), all recorded as 'drugs' in the DrugBank knowledgebase for the sake of simplicity (referred to hereafter as DPCCs, Fig. 1a and Supplementary Table 1). They can be categorized into three reaction types: nucleophilic addition, nucleophilic substitution, and oxidation (Fig. 1b)[20]. Subcategories include α, β-unsaturated ketone (**1**), α, β-unsaturated amide (**2**), acrylic aldehyde (**3**), acrylate (**4**), acrylonitrile (**5**), nitrosoureas (**6**), nitro (**7**), epoxide (**8**), halo-keto (**9**) and disulfide (**10**). These chemotypes have been either well-known to be cysteine-reactive or found to react with thiols or other nucleophiles on certain occasions. The average molecular weight of these DPCCs is 350 Da, with an average cLogP value of 2, and their properties comply with Lipinski's rule-of-five for drug-likeness (Fig. 1c)[21]. Additionally, 16 acrylamide-containing TCIs were included as controls (Supplementary Fig. 1).

In the initial assessment of the overall cysteinome reactivity of each drug, we performed QTRP experiments using HEK293T cell lysates (Fig. 2a). Specifically, the lysates were pre-treated with dimethyl sulfoxide (DMSO, vehicle control) or the drug (5 μM) for 2 h, followed by exposure to the broad-spectrum cysteine-reactive probe called IPM

(2-iodo-N-(prop-2-yn-1-yl) acetamide). Proteins harboring probe-labeled cysteines were then digested into tryptic peptides, which were conjugated to isotopically labeled biotin tags via copper-catalyzed alkyne azide cycloaddition reaction (CuAAC, also known as click chemistry) for enrichment. The enriched peptides were identified and quantified using liquid chromatography-tandem mass spectrometry (LC-MS/MS). Quantification of MS1 chromatographic peak ratios ($R_{H/L} = R_{DMSO:drug}$) for peptide pairs is used as a measurement for the ability of clinical covalent drugs competed cysteines residues. Each drug was screened in duplicate, yielding a total of 140 QTRP datasets (Supplementary Data 1).

We first evaluated the quality of the QTRP data. Notably, the profiling efficiency—defined as the percentage of identified peptides containing at least one probe-labeled cysteine—was generally greater than 90% (Supplementary Fig. 2a). In total, 18918 cysteines from 7170 proteins were quantified across all data sets, with a coefficient of variation (CV) lower than 40% in duplicates (Supplementary Fig. 2b). This represents a relatively high coverage of the human cysteinome as compared to previous reports (Supplementary Fig. 2c)[9,22].

We next measured the overall cysteinome reactivity for individual drugs by calculating the percentage of quantified cysteines with $R_{H/L}$ values ≥ 4 (herein referred to as engaged cysteines in vitro, indicating $\geq 75\%$ reduction in probe labeling). We found that, in general, the tested DPCCs interacted modestly with the HEK293T cysteinome, with an average reactivity of 4.8% (Fig. 2b). Similarly, 16 acrylamide-containing TCIs exhibited comparable cysteinome reactivity when applied at the same concentration (Supplementary Fig. 3a, b). However, principal component analysis (PCA) revealed that TCIs, but not DPCCs, clustered distinctly (Fig. 2c). These findings highlight the relative selectivity of TCIs compared to DPCCs, the latter of which are often discovered serendipitously rather than through targeted design. Additionally, our analysis identified 207 promiscuous cysteines that could be engaged by at least 10 drugs (Supplementary Fig. 4). These sites likely represent random-labeling events and should be avoided in future covalent drug discovery efforts.

It is important to note that target promiscuity observed with the tested DPCCs may not necessarily reflect their (poly-)pharmacology, as the analysis was conducted in non-physiological cell models using pharmacological concentrations. To clarify, the goal of this initial assessment was not to elucidate the mechanisms of action (MoAs) of the tested DPCCs, but to explore their potential as "drug-like" ligands that could expand the target space within the human proteome. In this context, we examined whether these drugs could engage cysteines in protein kinases, a critical class of druggable targets. We mapped the engagement profiles of both DPCCs and TCIs onto the Kinome tree and found that a large number of kinases
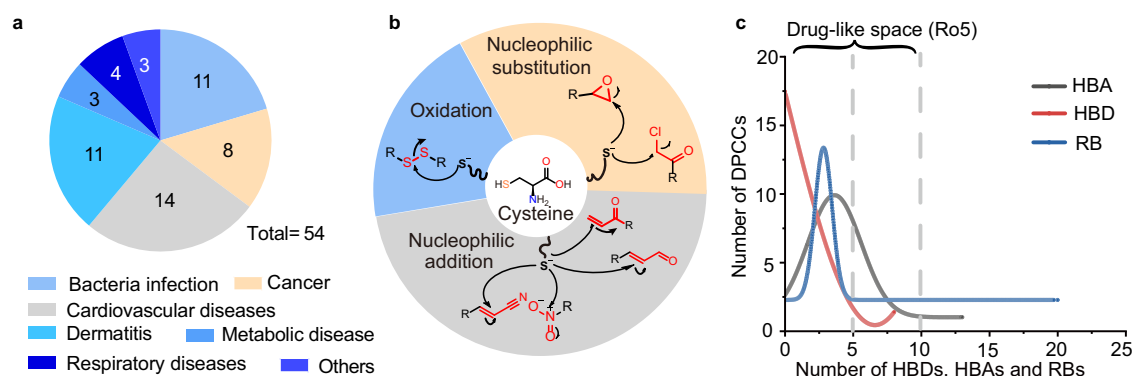

Fig. 1 | A library of drugs with potential cysteine-reactive chemotypes (DPCCs). **a** Categorization of DPCCs by their clinical indications. **b** Categorization of DPCCs by their potential reactivity mechanisms. **c** Distribution of DPCCs according to the number of hydrogen bond donors (HBDs), hydrogen bond acceptors (HBAs), and rotatable bonds (RBs).
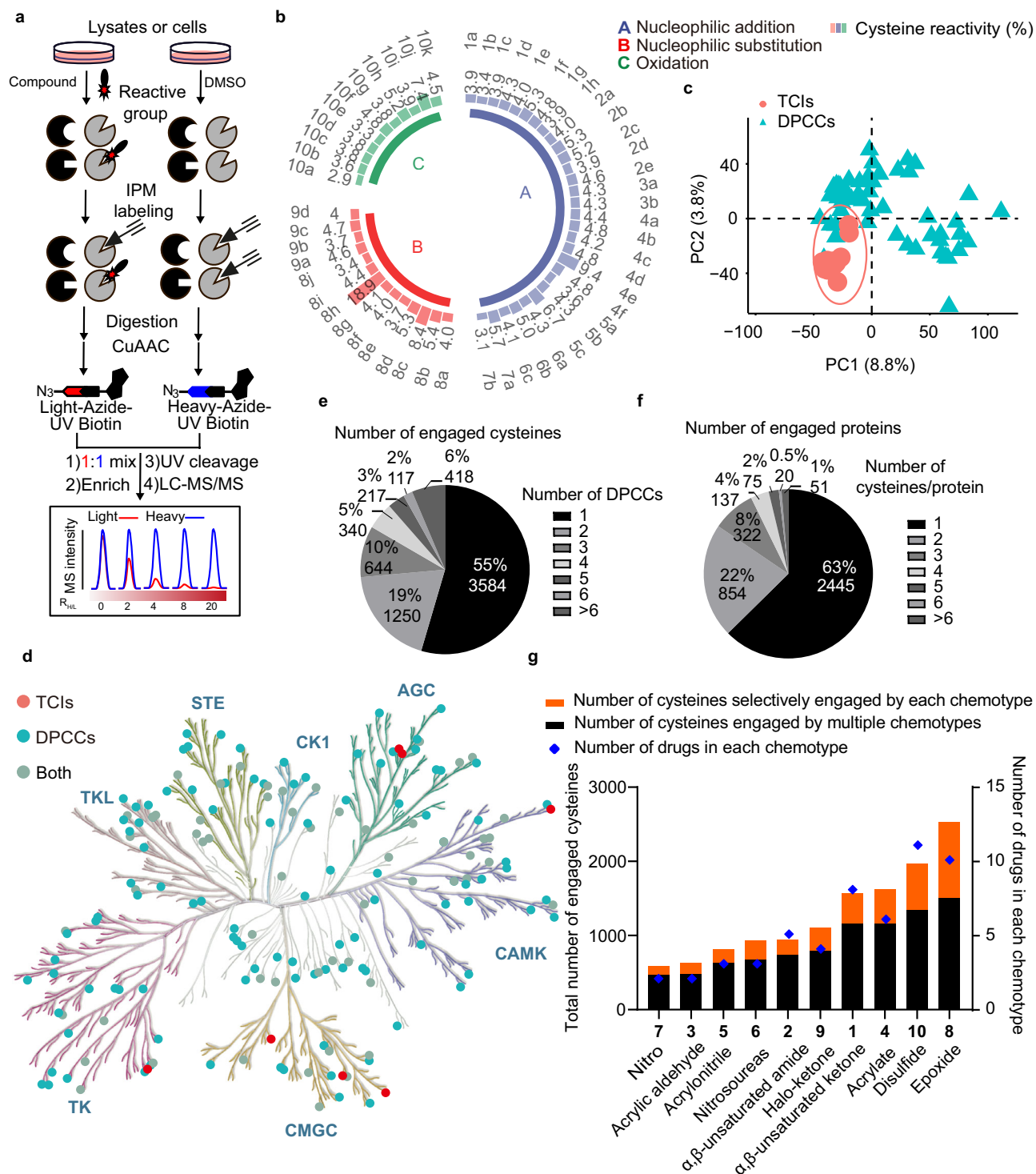
Fig. 2 | Screening the cysteinome reactivity of DPCCs at 5 µM concentration in vitro. a Schematic for QTRP experiments. **b** Radial bar chart summarizing the cysteine reactivity of each drug ($R_{H/L} \geq 4$). **c** PCA plot comparing the target profiles of DPCCs and TCIs. **d** Kinome tree showing the kinases engaged by DPCCs and TCIs, respectively. **e** Pie chart showing the number of DPCC hits per engaged cysteines. **f** Pie chart showing the number of engaged cysteines per protein. **g** Bar chart comparing the number of liganded cysteines for each chemotype, with red and black indicating cysteines engaged by single or multiple chemotypes, respectively.

were engaged by at least one DPCC, whereas TCIs targeted only a dozen of kinases (Fig. 2d).

We observed that 55% of the engaged cysteines were associated with only one DPCC, and ~63% of proteins contained only a single engaged cysteine (Fig. 2e, f), suggesting that cysteine engagement by DPCCs is often site-specific. To investigate whether the varying engagement profiles of DPCCs across the cysteinome could be

attributed to their diverse warheads and binding elements, we analyzed the reactivity of different chemotypes. These chemotypes engaged discrete sets of liganded cysteines and displayed marked differences in their overall cysteine reactivity (Fig. 2g). For instance, drugs with nitro (**7**) and acrylic aldehyde (**3**) warheads were the least reactive, while those with epoxide (**8**) were the most reactive. Despite these variations, PCA analysis revealed no clear chemotype-specific
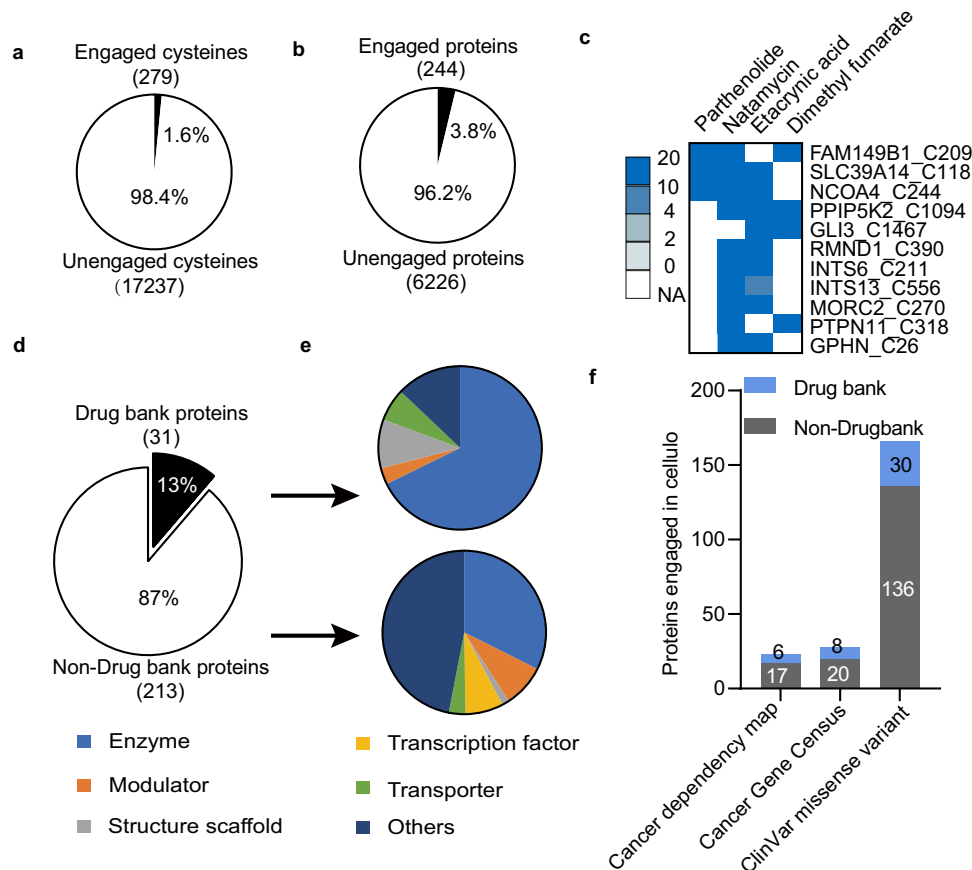
Fig. 3 | Profiling targets of DPCCs at 20 μM concentration in cells. a Fraction of all quantified cysteines targeted by DPCCs *in cellulo*. **b** Fraction of all quantified proteins targeted by DPCCs *in cellulo*. **c** Heat map showing $R_{H/L}$ values of 'hotspot' cysteines that can be engaged by at least two DPCCs. NA: not detected. **d** Fraction of all quantified proteins recorded in DrugBank. **e** Functional categorization of DrugBank and non-DrugBank proteins with DPCC-engaged cysteines. **f** Stacked column chart showing the number of DPCC-engaged proteins within each functional annotation.

clusters, and even acrylamide-based drugs did not group with TCIs (Supplementary Fig. 3c). This finding further highlights that the cysteinome reactivity is influenced by both the intrinsic reactivity of the drug warhead and its non-covalent binding properties. Moreover, the extent of cysteine engagement did not correlate with drug properties such as cLogP or molecular weight (Supplementary Fig. 5a, b), although cysteines ligandability was associated with the frequency of hydrogen bond donors (HBDs), hydrogen bond acceptors (HBAs), and rotatable bonds (RBs) in drug structures (Supplementary Fig. 5c–e). Overall, our study provides a comprehensive assessment of the engagement potential of a 70-member library of clinical covalent drugs, marking the largest survey of drug-cysteine interactions at the proteome-wide level. These findings also suggest that the site-specific target engagement for DPCCs may be attributed to multiple characteristics.

Profiling targets of DPCCs in cells

As mentioned earlier, almost all DPCCs, tested at 5 μM, exhibited modest reactivity with the cysteinome in vitro. Elevating treatment concentration to 500 μM did not significantly increase the overall cysteinome reactivity of most DPCCs except for etacrynic acid, dimethyl fumarate, parthenolide and natamycin (Supplementary Fig. 6, Supplementary Data 2). To assess the reactivity and selectivity of these four drugs in cells, we treated cells with each drug (20 μM) for 2 h *in cellulo* and then processed by QTRP. To enhance profiling depth, we incorporated an on-tip high-pH fractionation step into our workflow. This modification allowed the identification of an average of 18582 probe-labeled cysteines from 6705 proteins per drug. In total, we identified 24662 probe-labeled cysteines from 7853 proteins (Supplementary Data 3). We required cysteines to be quantified in at least two replicates and required their $R_{H/L}$-values to have a CV value lower than 40% for further interpretation, resulting in 17516 probe-labeled cysteines from 6470 proteins quantified (~8280 cysteines per drug). Notably, 704 cysteines previously unreported were detected (Supplementary Fig. 7a)[23,24], and 524 cysteines with $R_{H/L}$ values ≥ 2 were defined as initial target candidates. We also performed stable isotope dimethyl labeling-based quantitative proteomics to assess changes in protein abundance in drug-treated *versus* untreated cells. Although drug treatment altered protein abundance, only a small proportion of these changes were linked to initial target candidates (Supplementary Fig. 8a). After correcting for protein abundance shifts, we identified 279 cysteines with a ratio of $R \geq 2$ and significant intensity differences (*p* value < 0.05) as high-confidence target candidates (Supplementary Fig. 8b), representing 1.6% and 3.8% of the total cysteines and proteins, respectively (Fig. 3a, b). Of these, only ~20% drug-engaged cysteines could be recorded previously as targets of fragment-based covalent ligands (Supplementary Fig. 7b)[23,24], emphasizing the need for more comprehensive chemical scaffolds to expand the ligandable cysteinome. Furthermore, we mapped "hot spots" (i.e., cysteines engaged by multiple drugs) onto a small subset of proteins (Fig. 3c), with the majority (~93%) of proteins having only one liganded cysteine.

Only a modest fraction (13%) of proteins with engaged cysteines were recorded in the DrugBank knowledgebase (Fig. 3d), indicating that these DPCCs target many proteins that lack existing chemical modulators. DrugBank proteins with DPCC-engaged cysteines were mainly enzymes, channels and transporters, while non-DrugBank

proteins included adapter/scaffolding proteins and transcription factors, which are traditionally difficult to target with small molecules (Fig. 3e). Additionally, we investigated the disease relevance of DPCC-engaged proteins by cross-referencing multiple disease-related protein annotation resources (Fig. 3f, Supplementary Data 3). We found that 6 DrugBank and 17 non-DrugBank proteins were recorded in a cancer dependency map, which includes 769 genes differentially required in cancer cell lines[25]; 8 DrugBank and 20 non-DrugBank proteins as cancer-driving factors according to the Cancer Gene Census (CGC); 30 DrugBank and 136 non-DrugBank proteins with ClinVar missense variants potentially contributing harmful disease phenotypes. These findings, along with functional annotations, could help prioritize future therapeutic target.

To demonstrate the utility of this resource, we present three case studies: First, we identified a cysteine-directed interaction with tyrosine Janus kinase 1 (JAK1), a known target for immun(onc)ological therapies. Second, we uncovered a "hot spot" on nuclear receptor coactivator 4 (NCOA4), a protein never before shown to be druggable. Lastly, we explored a DPCC-cysteine interaction within an E3 ligase, offering a promising strategy for developing proteolysis-targeting chimeras (PROTACs).

Expanding the engagement profile on a known drug target

In our initial effort to assess the functional impact of DPCC-cysteine interactions identified *in cellulo* through QTRP experiments, we focused on JAK1, a member of the non-receptor Janus tyrosine kinase family. The combination of JAK enzymes and seven Stat (signal transducers and activators of transcription) transcription factors is central to cytokine receptor signaling, which regulates diverse biological and disease processes[26]. For example, JAK1 is essential for IL4-Stat6 signaling and IFNα-Stat1 signaling (Fig. 4a)[27]. Given the crucial role of JAKs in immune and inflammatory diseases, JAK inhibitors have been developed, with drugs like tofacitinib, upadacitinib, and itacitinib receiving FDA approval. However, all these inhibitors act via an orthosteric (ATP-competitive) mechanism, binding to the conserved ATP pocket, making it challenging to develop isoform-selective JAK inhibitors. A promising strategy to overcome selectivity issues is targeting allosteric sites in kinases[28,29].

Among the seven cysteines mapped on JAK1 by DPCCs, only C988 was sensitive to natamycin, a macrolide polyene antibiotic (Fig. 4b, c). We first confirmed that natamycin blocked biotinylated thiol probe labeling of Flag epitope-tagged wild type JAK1 in HEK293T cells (Fig. 4d). However, the mutation of JAK1 at position C988 to serine resulted in a reduction of labeling signals, which were unaffected by natamycin (Fig. 4d). To further verify this interaction, we synthesized an alkyne-functionalized analog of natamycin (Natamycin-Alkyne, Fig. 4e), which confirmed that natamycin directly targeted JAK1 (Fig. 4f). This interaction was competed by natamycin and abrogated in the C988S JAK1 mutant. Notably, previous studies have shown that JAK1 C988 is targeted by diverse electrophiles[10,22,30–33], even though this site is a solvent-inaccessible with a pPSE (amino acid side-chain accessibility) value of 12[24]. These findings suggest that JAK1 C988 is a "hot spot" for ligand engagement.

Since C988 of JAK1 is not in the ATP binding pocket, we explored whether the covalent binding of natamycin to JAK1 could affect its kinase activity via an allosteric mechanism. Using CorrSite2.0, a computational tool with over 90.0% prediction accuracy for detecting allostery pockets[34], we identified that C988 is localized in one such pocket (Z-score > 0.5, Fig. 4g). However, natamycin did not inhibit the catalytic activity of recombinant JAK1, as assessed by ATP consumption using the ADP-Glo™ Kinase Assay or direct substrate phosphorylation measurement through the PhosphoSens® Protein Kinase Assay. In contrast, the orthosteric JAK inhibitor tofacitinib strongly inhibited JAK1 activity. Moreover, natamycin did not enhance the potency of tofacitinib in these assays (Fig. 4h, Supplementary Fig. 9a, b).

Interestingly, despite not inhibiting JAK1 catalytic activity in vitro, natamycin treatment (20 μM, 4 h) attenuated IL-4-induced activation of the JAK1-Stat6 pathway and IFNα-induced activation of the JAK1-Stat1 pathway in cells (Fig. 4i, j). These inhibitory effects were abolished by mutations at C988 (C988S or C988V) in HEK293T cells (Fig. 4k-l, Supplementary Fig. 9c, d, Supplementary Fig. 10 and Supplementary Fig. 11). Taken together, these results suggest that C988 in JAK1 is likely a ligandable allosteric site, potentially offering a new strategy for targeting this important therapeutic protein. Notably, during the preparation of this work, Cravatt and colleagues reported another ligandable allosteric cysteine, C817 in JAK1[35], further supporting the utility of chemoproteomics in expanding the engagement profile of known drug targets.

Discovering the functional "hot spot" on an undruggable protein

We next prioritized non-DrugBank proteins for functional analysis, especially those whose engaged cysteines were located in poorly characterized domains. One such target was nuclear receptor coactivator 4 (NCOA4), a cargo receptor of ferritin heavy chain FTH1, which plays a key role in iron storage and metabolism (Fig. 5a)[36]. Notably, C244 of NCOA4 was a 'hot spot', targeted by three DPCCs: parthenolide, natamycin and etacrynic acid (Fig. 5b, Supplementary Fig. 12a). We confirmed that these drugs blocked biotinylated thiol probe labeling of Flag epitope-tagged wild type NCOA4. However, the mutation of NCOA4 at position C244 to serine resulted in a reduction of labeling signals, which were unaffected by these drugs. (Fig. 5c, Supplementary Fig. 12b). To investigate how these DPCCs might modulate the function of NCOA4 in cells, we first examined the effect on FTH1 levels. Treatment with these drugs resulted in a concentration-dependent increase in FTH1 protein levels (Fig. 5d, Supplementary Fig. 12c and Supplementary Fig. 13, 14), without significantly altering FTH1 mRNA levels (Fig. 5e, Supplementary Fig. 12d). Additionally, we found that the NCOA4-FTH1 interaction could be disrupted by parthenolide and other two DPCCs (Fig. 5f, Supplementary Fig. 12e). To confirm that these effects were due to C244 engaging by these drugs, we transiently expressed either the wildtype (WT) or C244S mutant NCOA4 in HEK293T cells. As expected, this C244S mutation significantly reduced the impact of parthenolide or other two DPCCs on FTH1 protein levels and its interaction with NCOA4 (Fig. 5f-g, Supplementary Fig. 12e, f). Similarly, knockdown of NCOA4 abolished the effects of these DPCCs on FTH1 protein levels (Fig. 5h, Supplementary Fig. 12g).

Given that the NCOA4-FTH1 interaction is essential for ferritinophagy[37], we next investigated whether these DPCCs could inhibit the release of free irons and ferroptosis. As expected, treatment with parthenolide or other two DPCCs decreased the intracellular level of free Fe^{2+}, as measured by the selective fluorescent probe FerroOrange. This effect mimicked that of deferoxamine (DFO), a known iron-chelating agent (Fig. 5i, Supplementary Fig. 12h). Considering the regulatory role of reactive oxygen species (ROS) in ferritinophagy[38], we investigated whether such pharmacological effects were linked to redox stress, if any. We found that none of the three drugs tested increased ROS levels in cells (Supplementary Fig. 15a, Supplementary Fig. 16). Furthermore, the changes in FTH1 expression and free iron levels induced by these drugs were not mitigated by NAC, an antioxidant that neutralizes ROS (Supplementary Fig. 15b, c). These results indicate that the observed ferritinophagy is probably driven by the covalent interaction between the drug and its target, rather than oxidative stress. Additionally, overexpression of wild type NCOA4 increased mRNA levels of PTGS2, a molecular marker of ferroptosis[9,39], and lipid peroxidation, which was measured using the sensitive dye called BODIPY-C11 (Fig. 5j, k, Supplementary Fig. 12i, j). Both markers of ferroptosis[40] were reduced upon treatment with parthenolide or other two DPCCs. Notably, the NCOA4 C244S mutation attenuated these
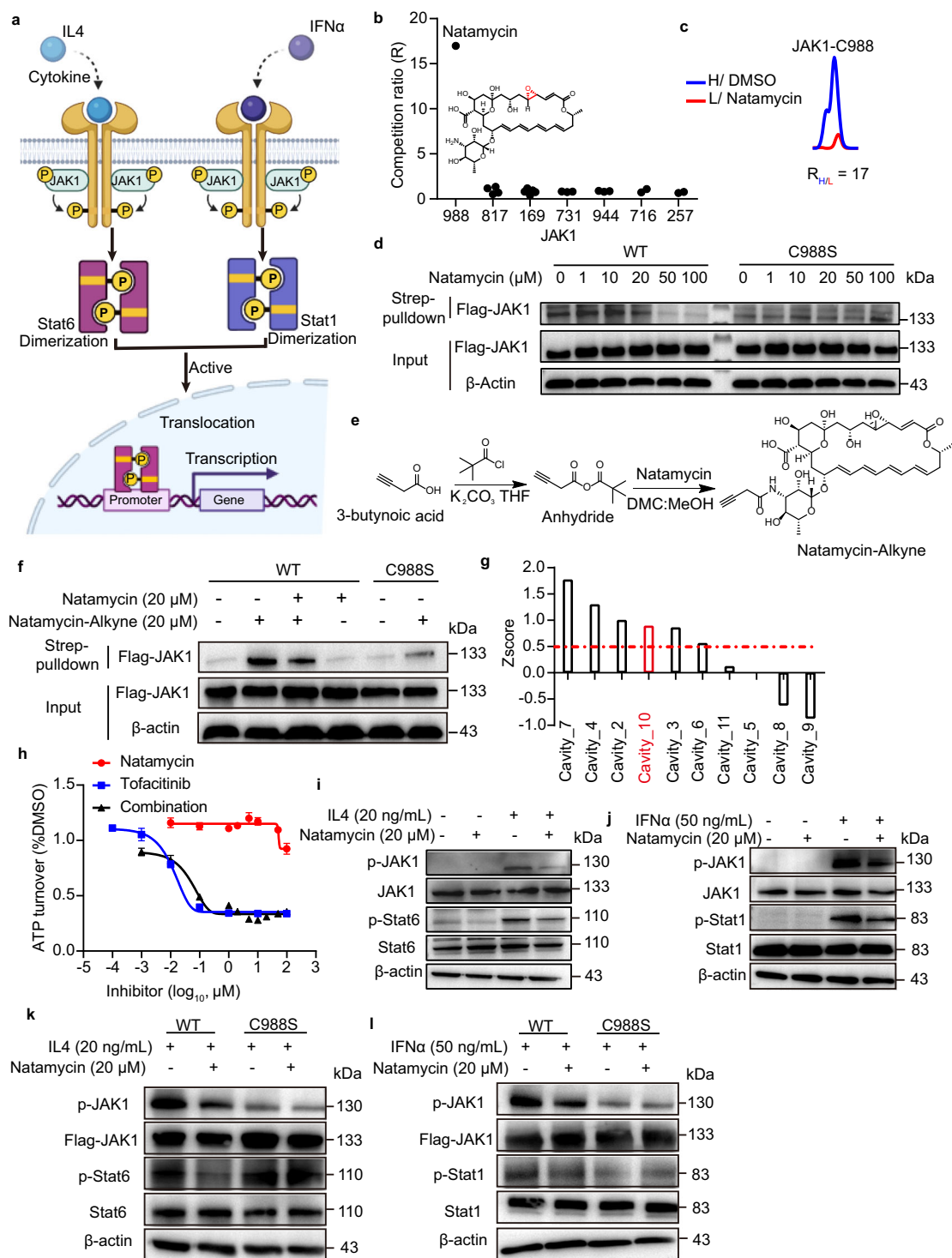
inhibitory effects (Fig. 5j, k, Supplementary Fig. 12i, j). Furthermore, overexpression of wild type NCOA4, but not the C244S mutant, led to increased cell survival following DPCC treatment (Fig. 5l, Supplementary Fig. 12k). Taken together, these results suggest that the biological activity of parthenolide, natamycin, and etacrynic acid in cells may, at least in part, be attributed to downregulation of the NCOA4-FTH1-Fe^{2+} axis, specifically through targeting C244 of NCOA4. More broadly, this functionally important cysteine may serve as a valuable ligandable site for the design of more potent and selective covalent inhibitors of ferroptosis.

Repurposing a covalent drug as a E3 ligase recruiter for targeted protein degradation

PROTAC has emerged as a promising drug discovery model, where thalidomide-type motifs are used to recruit E3 ligases (e.g., cereblon, VHL) to target proteins for degradation via a ubiquitin-proteasome-dependent manner[41]. One major challenge, however, is that only ~1% of the approximately 600 E3 ligases has been utilized in targeted protein degradation[42]. Recently, a number of covalent recruiters of E3 ligases have been uncovered, including electrophilic ligands KB02 and EN106 for DCAF16 and FEM1B, respectively[43,44], as well as electrophilic natural

Fig. 4 | Expanding the engagement profile on a known drug target. a Schematic showing the canonical JAK1/Stat6 and JAK1/Stat1 pathways, triggered by cytokines (IL4) and (IFNα), respectively. The elements are obtained from Biorender. **b** Dot plot showing the $R_{H/L}$ values for all quantified cysteines of JAK1, highlighting C988 as the sole engaged site. Each data point represents a unique DPCC-cysteine interaction quantified via QTRP from 3 biological replicates and 2 technical replicates. **c** Representative XIC showing the change in probe-labeled JAK1^{C988} from cells treated with or without Natamycin, with light and heavy-labeled peptide profiles shown in red and blue, respectively. The average $R_{H/L}$ values from four replicate experiments are indicated below the XIC. **d** Representative western blot analysis showing the competition of Natamycin against biotin-iodoacetamide (100 μM, 1 h) labeling of JAK1. HEK293T cells overexpressing JAK1 and the C988S mutant were treated with varying concentrations of Natamycin for 4 h. The immunoblots are representative of three independent experiments. **e** Synthesis of Natamycin-Alkyne. **f** Representative western blots showing the labeling of JAK1 or JAK1-C988S with Natamycin-alkyne *in cellulo*, with a decrease observed in the presences of the parent compound. The immunoblots are representative of three independent experiments. **g** CorrSite2.0-based prediction showing that JAK1^{C988} is localized within a potential allosteric pocket. **h** In vitro activity of Natamycin, Tofacitinib (Tofa), and their combination against recombinant JAK1 (residues 438–1154). Data are presented as mean ± s.d. from three independent experiments. **i** Representative western blots showing the effects of Natamycin on JAK1 phosphorylation (p-JAK1 at Y1034/Y1035), as well as IL-4-stimulated Stat6 phosphorylation (p-Stat6 at Y641 phosphorylation). **j** Representative western blots showing the effects of Natamycin on JAK1 phosphorylation (p-JAK1 at Y1034/Y1035), IFNα-stimulated Stat1 phosphorylation (p-Stat1 at Y701). **k** Representative western blots showing that the C988S mutation abrogates the inhibitory effect of Natamycin on the IL4/JAK1/Stat6 pathway. **l** Representative western blots showing that the C988S mutation abolished the inhibitory effect of Natamycin on the IFNα/JAK1/Stat1 pathway. Quantification results from three independent experiments for (**i**–**l**) are provided in Supplementary Fig. 10. Source data are provided as a Source Data file.
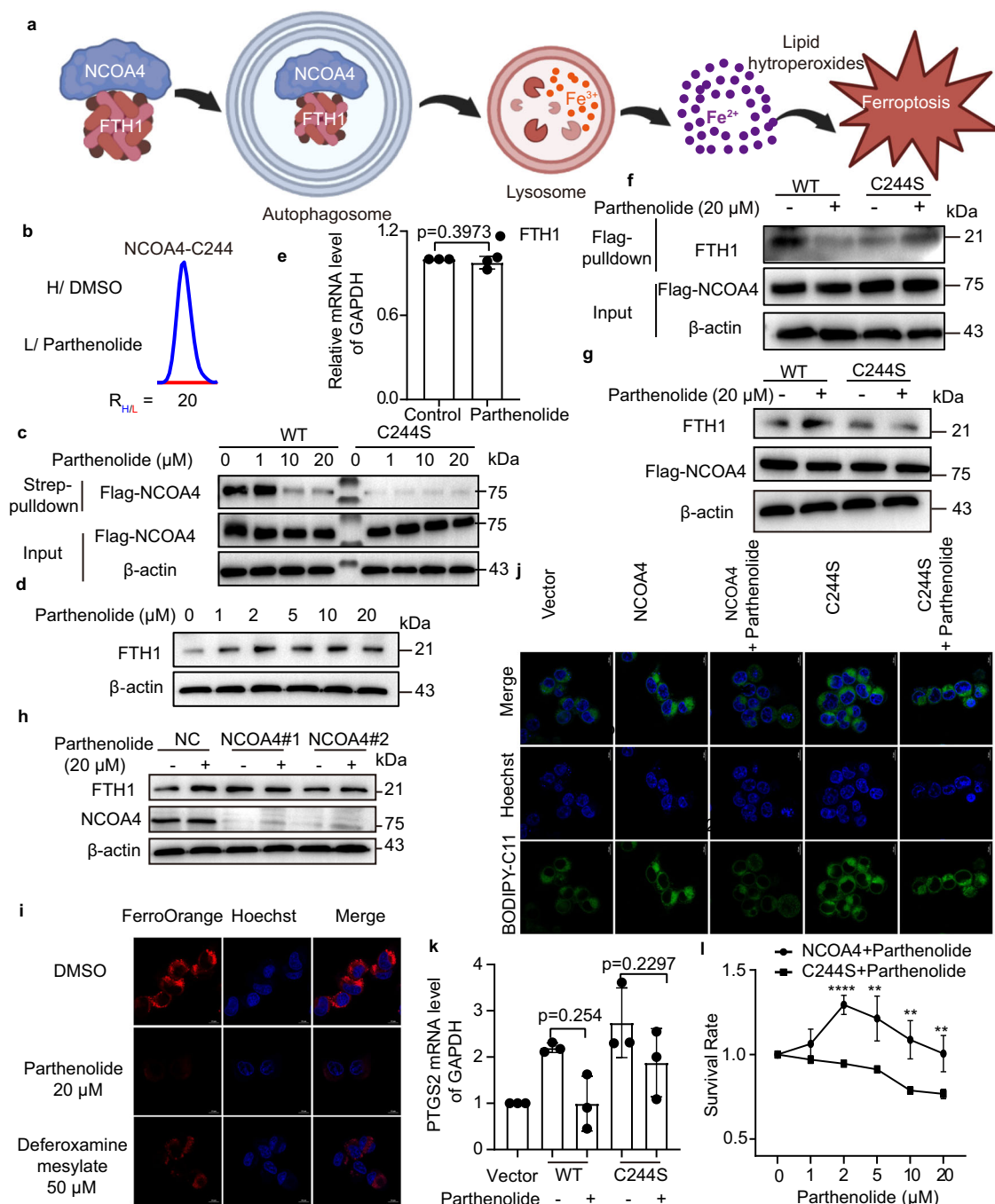
Fig. 5 | Discovering the functional 'hot spot' on an undruggable protein.
a Schematic of NCOA4 transporting FTH1 to the lysosome for degradation, followed by the induction of ferroptosis. The elements are obtained from Biorender. **b** Representative XICs showing changes in probe-labeled NCOA4^C244. The profiles for light- and heavy-labeled peptide are shown in red and blue, respectively. Average $R_{H/L}$ values from four replicates are displayed below the XIC. **c** Representative western blot analysis of DPCCs competition against biotin-iodoacetamide (100 μM, 1 h) labeling of NCOA4. HEK-293T cells overexpressing NCOA4 or NCOA4^C244S were treated with indicated drugs for 4 h. The immunoblots are representative of three independent experiments. **d** Representative western blots showing FTH1 expression in HT1080 cells upon titration of parthenolide at indicated concentrations. **e** Bar chart showing the effects of parthenolide (20 μM, 6 h) on FTH1 mRNA expression levels in HT1080 cells. Data are mean ± s.d. (n = 3, two-sided Student's t-test, a p value less than 0.05 is considered statistically significant, the same below). **f** Representative immunoprecipitation-western blot results demonstrating that parthenolide treatment (20 μM, 6 h) inhibited the NCOA4-FTH1 interaction. Protein binding to FLAG-NCOA4 expressed heterologously in HEK293T cells with or without parthenolide treatment was subjected to anti-FLAG enrichment, separated with SDS-PAGE, and detected using indicated antibodies. **g** Representative western blots showing that the C244S mutation

abolished the effect of parthenolide-induced upregulation of FTH1.
h Representative western blots showing that siRNA-mediated knockdown of NCOA4 abrogated the parthenolide-induced upregulation of FTH1 in HT1080 cells. **i** Representative immunofluorescence images showing that parthenolide treatment (20 μM, 6 h) reduced the level of free Fe^{2+} in HT1080 cells, as measured by FerroOrange (red). Nuclei were stained with Hoechst 33342 (blue). Scale bars represent 10 μm. DFO was used as a positive control. **j** Representative immunofluorescence images showing that parthenolide treatment (20 μM, 6 h) reduced lipid peroxidation levels in HEK293T cells overexpressing wild-type NCOA4, but not in cells expressing the C244S mutant. Lipid peroxidation was measured by BODIPYC11. Nuclei were stained with Hoechst 33342 (blue). Scale bars represent 10 μm. **k** Bar chart showing the effect of parthenolide (20 μM, 6 h) on PTGS2 mRNA expression levels in HEK293T cells overexpressing wild-type NCOA4 or the C244S mutant. Data are mean ± s.d. (n = 3, two-sided Student's t-test). **l** Survival rates of HEK293T cells expressing wild-type and C244S mutant NCOA4 upon parthenolide treatment, as measured by MTT assay, Data are mean ± s.d. (n = 6, Multiple t-test, ****p = 0.000019, **p = 0.004088, **p = 0.002039, **p = 0.005044). Quantification results from three independent experiments for (**d**, **f**–**j**) are shown in Supplementary Fig. 13. Source data are provided as a Source Data file.

products nimbolide and piperlongumine for RNF114 and KEAP1, respectively[45,46]. Despite these advances, the pharmacokinetic properties and safety profiles of these covalent recruiters—derived from electrophilic ligands and natural products—remain largely unknown, hindering further development. In this context, we reasoned that DPCCs, which have favorable pharmacokinetic properties and well-documented safety profiles, could serve as a novel class of E3 ligase recruiters.

Our *in cellulo* QTRP experiments indeed identified a number of DPCC-E3 ligase interactions (Fig. 6a). Notably, many E3 ligases, previously lacking specific recruiters, were covalently engaged by etacrynic acid or parthenolide. Among these, etacrynic acid particularly caught our attention because it is an oral loop diuretic with approximately 100% bioavailability[47]. Furthermore, compared to previously reported covalent recruiters, etacrynic acid is more water-soluble and possesses a carboxy group (pKa ~3.8), which facilitates its linkage to protein-targeting ligands. As a proof-of-concept, we conjugated etacrynic acid to the bromodomain and extra-terminal (BET) family inhibitor (S)-JQ1 through a one-step reaction, resulting in a PROTAC reagent termed EtA-(S)-JQ1 (Fig. 6b).

As anticipated, treatment with EtA-(S)-JQ1 in HEK293T cells led to the degradation of endogenous BRD4 within 4 h in a concentration-dependent manner, as measured by Western blot. Notably, BRD4 expression was significantly reduced at concentrations of EtA-(S)-JQ1 as low as 100 nM (Fig. 6c, Supplementary Fig. 17a), while no changes were observed in BRD4 mRNA levels (Fig. 6d). Additionally, BRD4 degradation induced by EtA-(S)-JQ1 was attenuated by the competition of its parent drug etacrynic acid, suggesting that EtA-(S)-JQ1 binds to the same target (Fig. 6e). Pre-treatment with bortezomib (BTZ, a proteasome inhibitor) also attenuated EtA-(S)-JQ1-mediated BRD4 degradation, confirming that degradation is mediated by the proteasome system (Fig. 6e, Supplementary Fig. 18a and Supplementary Fig. 17b, c). When compared to MZ1, a previously reported JQ1-based non-covalent degrader[48], EtA-(S)-JQ1 showed enhanced BRD4 degradation at the same treatment conditions (100 nM, 4 h) (Fig. 6f, Supplementary Fig. 17e, g and Supplementary Fig. 18b). We synthesized two control compounds to further validate our findings (Fig. 6g): 1) Compound **11**, a non-covalent version of EtA-(S)-JQ1; 2) Compound **12**, a version of EtA-(S)-JQ1 containing the (R)-JQ1 enantiomer, which does not bind to BRD4. As expected, neither negative control induced BRD4 degradation (Fig. 6h, Supplementary Fig. 17d, 17f and Supplementary Fig. 18c), confirming that BRD4 degradation by EtA-(S)-JQ1-mediated is driven by covalent interaction.

To assess the proteome-wide impact and selectivity of EtA-(S)-JQ1, we conducted a stable isotope dimethyl labeling-based quantitative

proteomic analysis to measure changes in protein expression induced by EtA-(S)-JQ1 compared to control treatments (Fig. 6i, Supplementary Fig. 18d, Supplementary Data 4). Similar to other JQ1-based covalent degraders[43–45], EtA-(S)-JQ1 selectively degraded BRD4 rather than BRD2 or BRD3, despite JQ1 being a pan inhibitor of the BET bromodomain[49]. Nonetheless, we identified a dozen of non-BET proteins as putative off-targets among ~6000 quantified proteins. It is not unexpected since even highly selective PROTACs may degrade off-targets in complex proteomes that were untouched by their parent inhibitors[42].

Next, we tested whether EtA-(S)-JQ1-mediated BRD4 degradation was triggered through the recruitment of the E3 ligase HECTD1. HECTD1, a member of HECT (Homologous to E6AP C-Terminus) domain E3 ligases, regulates various biological processes[50,51]. Interestingly, the etacrynic acid-engaged C1368 of HECTD1 is spatially distant from the active site (C2579) of this E3 ligase, according the predicted 3D structure by AlphaFold2 (Fig. 6j)[52]. This suggests that the interaction is unlikely to interfere with the enzymatic activity of HECTD1. To verify that BRD4 degradation was mediated by HECTD1, we found that BRD4 degradation was attenuated in HECTD1 knockdown HEK293T cells compared to wild-type cells, while knockdown of DCFA16, another E3 responsible for many covalent PROTACs[43,53], could not afford the same effect (Fig. 6k, l and Supplementary Fig. 17h, k). Moreover, the C1368S HECTD1 mutant abolished the effect of EtA-(S)-JQ1 (100 nM, 4 h)-induced BRD4 degradation in HEK293T cells (Fig. 6m and Supplementary Fig. 17l, m). Taken together, these results demonstrate that the covalent engagement of HECTD1 by etacrynic acid can be harnessed for targeted protein degradation, offering a strategy for PROTAC development.

Discussion

Recognizing a growing interest in the development of covalent drugs in both academia and industry, we felt that a systematic analysis was crucial for assessing the proteome-wide reactivity and selectivity of these drugs, especially at the site-level resolution. Here, we present a large-scale chemoproteomic analysis to define the target landscape of 70 DPCCs in the native cell lysates and/or in intact cells. The data generated from this analysis provides valuable insights that are often not achievable with smaller datasets, offering unique opportunities for chemical biologists and medicinal chemists alike.

Our findings adds further complexity of the known polypharmacological profiles of several DPCCs (*incl.* GAPDH[2], GSDMD[3] RSK2[4], IRAK4[5] and PRKCQ[6] for dimethyl fumarate; FAK1, IKK-β, Hsp72 and TrxR for parthenolide; GSTM1[54] and ADT3[55] for etacrynic acid, Supplementary Table 1). Notably, we also uncovered previously unknown target promiscuity for many others, whose mechanisms of
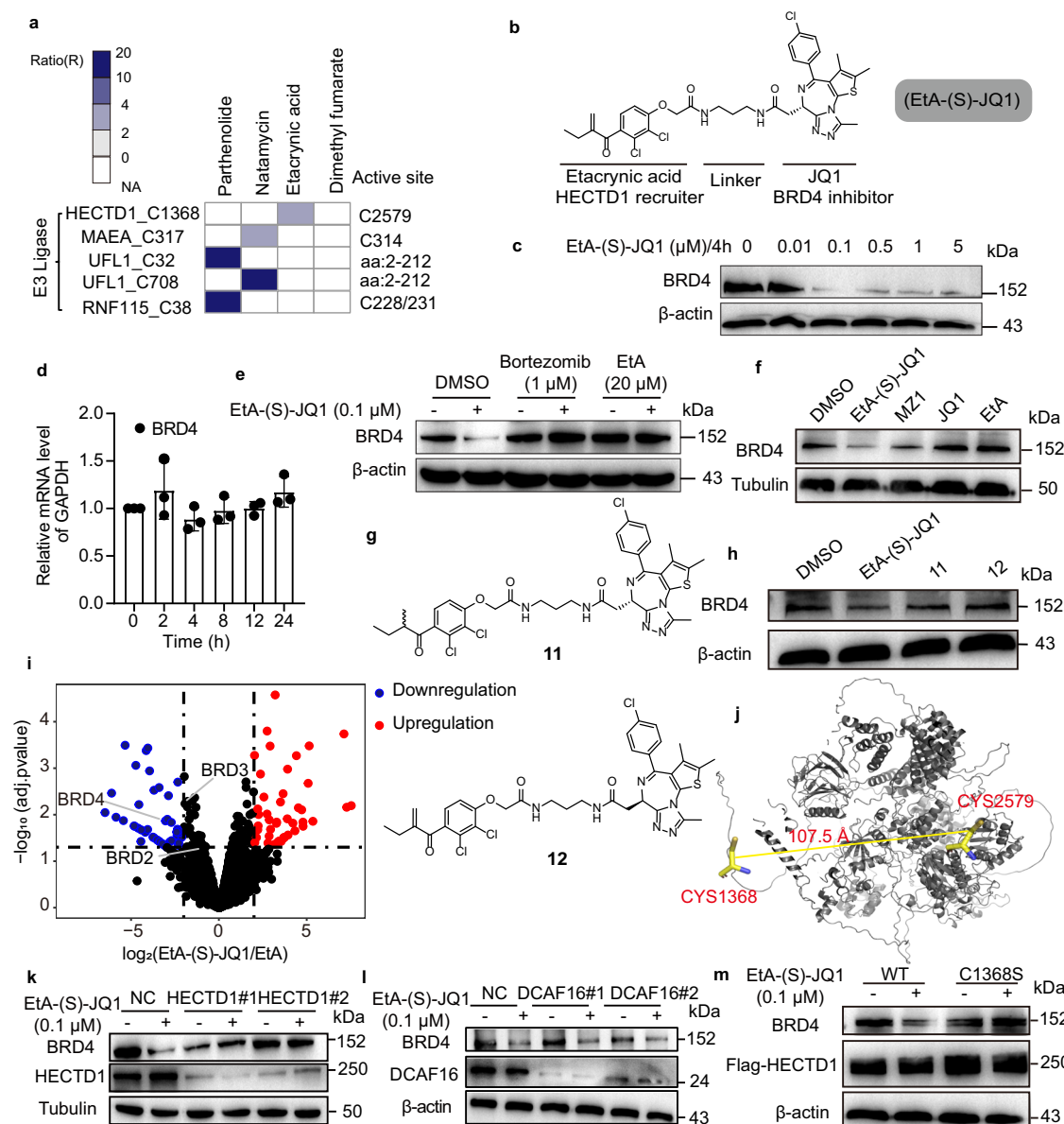
Fig. 6 | Repurposing etacrynic acid as an E3 recruiter for targeted protein degradation. a Heat map showing $R_{H/L}$ values of representative cysteines engaged onto E3 ubiquitinating enzymes. NA: not detected. **b** Chemical structure of EtA-(S)-JQ1. **c** Representative western blots showing the effect of EtA-(S)-JQ1 treatment on BRD4 expression in HEK293T cells. **d** Bar chart showing the effect of EtA-(S)-JQ1 (100 nM) on BRD4 mRNA expression levels in HEK293T cells over the indicated time points. Data are mean ± s.d. ($n = 3$, two-sided Student's t-test, $p < 0.05$ considered significant). **e** Representative western blots showing that bortezomib or etacrynic acid attenuated EtA-(S)-JQ1-mediated BRD4 degradation. HEK293T cells were pre-treated with DMSO, the proteasome inhibitor bortezomib (BTZ) (1 μM, 2 h) or etacrynic acid (20 μM, 2 h), followed by EtA-(S)-JQ1 treatment (100 nM, 4 h). **f** Representative western blots showing that EtA-(S)-JQ1, but not JQ1 (20 μM, 4 h), induced BRD4 degradation in HEK293T cells. MZ1 was used as a positive control. **g** Chemical structures of **11**, a non-covalent version of EtA-(S)-JQ1, and **12**, the same molecule as EtA-JQ1 but with the (R)-(-)-JQ1 enantiomer as the binding moiety.

h Representative western blots showing that EtA-(S)-JQ1, but not JQ1 (20 μM, 4 h), nor **11/12**, induced BRD4 degradation in HEK293T cells. **i** Volcano plot showing the $\log_2$ ratio of the EtA and EtA-(S)-JQ1 (5 μM) treated channels and the $-\log_{10}(adj.$ $pvalue$) for all quantified proteins ($n = 3$, LIMMA-test). **j** Mapping of EtA-(S)-JQ1-engaged cysteine (C1368) and active site cysteine (C2579) on the 3D structure of HECTD1, predicted by AlphaFold2. **k** Representative western blots showing the effect of *hectd1* knockdown on EtA-(S)-JQ1 (100 nM, 4 h)-induced BRD4 degradation in HEK293T cells. **l** Representative western blots showing the effect of *dcaf16* knockdown on EtA-(S)-JQ1 (100 nM, 4 h)-induced BRD4 degradation in HEK293T cells. **m** Representative western blots showing that the C1368S mutation of HECTD1 abolished EtA-(S)-JQ1 (100 nM, 4 h)-induced BRD4 degradation in HEK293T cells (100 nM, 4 h). Quantification data from three independent experiments for panels (**c, e, f, h, k–m**) are provided in Supplementary Fig. 17. Source data are provided as a Source Data file.

action had remained poorly understood. Using a combination of biochemistry and chemical biology approaches, we validated several drug-target interactions and identified ligandable cysteines on both DrugBank and Non-DrugBank proteins. Despite these advancements, understanding how most newly identified cysteine engagements affect protein functions remains a technical challenge. We anticipate that combining our data with genetic and computational approaches[56,57]

will help prioritize essential cysteines for future covalent drug discovery. Furthermore, mapping the DPCC-target landscape in pathophysiological-relevant models will be crucial for explaining side effects and offering new avenues drug repurposing[58,59].

Another significant aspect of our study is the opportunity to make a head-to-head comparison between rationally designed covalent drugs (i.e., TCIs) and those discovered by serendipity (i.e., DPCCs).

Unsurprisingly, most DPCCs exhibit target promiscuity, which could have both advantageous and detrimental therapeutic consequences. This promiscuity, however, appears to be shared by most DPCCs, even those with cysteinome reactivity similar to TCIs. In contrast, the target landscape of individual TCIs tends to be more specific, and our dataset could serve as a reference for evaluating the proteome-wide selectivity of other TCIs currently under development.

Our data, in conjunction with recent reports[14,35,60], also highlight the utility of chemoproteomics for identifying allosteric sites that are difficult to detect with traditional methods. Interestingly, most cysteines covalently targeted by DPCCs are not located at active sites. These cysteines may represent potential allosteric sites, which are highly relevant for drug discovery, as targeting such sites could increase drug selectivity. For instance, our analysis identified a ligandable allosteric cysteine in JAK family proteins, which may enable the development of novel pan-JAK inhibitors.

Moreover, our analysis underscores the potential for clinical covalent drugs to target protein-protein interactions (PPIs). For example, we demonstrate that parthenolide disrupts the NCOA4-FTH1 interaction by covalently modifying a cysteine (C244) located in an intrinsically disordered region of NCOA4. Notably, this site is distinct from the C-terminal element of NCOA4, which has been identified as critical for FTH1 binding[37] and targeted by non-covalent inhibitors[61]. The modification of C244 by parthenolide likely induces a conformational change in NCOA4, thereby disrupting the PPI rather than competing for the traditional binding site. Moreover, by utilizing the interactome database[62], we were able to map 17 drug-targeted cysteines onto PPI interfaces (Supplementary Table 2). While the functional importance of these interactions remains to be fully explored, they represent promising targets for future drug discovery.

Lastly, our findings address a key challenge in PROTAC development: balancing drug-likenesses with potency and selectivity. To date, the most widely used E3 ligase recruiter for designing PROTACs was derived from thalidomide, an immunomodulatory drug[42]. Despite researchers continuing to churn out new variants, their 'drug-like' properties remain underexplored. We propose that exploring other approved drugs for recruiters may offer a more efficient approach. Our discovery covalent drug-cysteine interactions, particularly with ethacrynic acid, presents a strategy for targeted BRD4 degradation. However, further investigation is needed to determine whether this approach is effective in vivo and applicable to other drug targets.

In summary, our comprehensive chemoproteomic analysis uncovers a wide range of unprecedented binding events by clinical covalent drugs, targeting both known therapeutic targets and those traditionally difficult to address with small molecules. This extensive dataset not only opens avenues for discovering novel allosteric sites, intrinsically disordered regions, and PPI interfaces for covalent drug discovery, but also holds promise for drug repurposing, including identifying recruiters for targeted protein degradation.

Methods

Reagents and antibodies

Drugs were purchased from J&K Scientific, Cayman, Selleck, Sigma, and Targetmol; Iodoacetamide (cat. No. V900335), tris[(1-benzyl-1H-1,2,3-triazol-4-yl) methyl] amine (TBTA) (cat. No. 678937), and sodium ascorbate (cat. No. A7631) were purchased from Sigma-Aldrich. Dithiothreitol (DTT, cat. No. A620058-0025) was purchased from BBI Life Sciences; Light azido-UV-biotin (cat. No. EVU102), and heavy azido-UV-biotin (cat. No. EVU151) were purchased from KeraFast; Sequencing-grade trypsin (cat. No. V5113), JAK1 Kinase enzyme system (VA7207) and ADP-Glo™ Kinase Assay Kit (V6930) were purchased from Promega; PhosphoSens® Protein Kinase Assay (CSKS-AQT0663K) were purchased from AssayQuant Technologies Inc.; Streptavidin sepharose beads (cat. No. 17-5113-01) were purchased from GE; Tofacitinib (T6321) was purchased from Targetmol; FerroOrange was purchased from

Dojindo (F374); BODIPY-C11 was purchased from Invitrogen (D3861); Deferoxamine mesylate (DFO, T1637) was purchased from Targetmol; N-acetyl-L-cysteine (NAC, A9165) was purchased from Sigma; Reactive Oxygen Species Assay Kit (CA1420) was purchased from Solarbio®Life Sciences; Rabbit polyclonal Anti-Stat6 (51073-1-AP, 1:1000), Mouse monoclonal Anti-JAK1 (66466-1-Ig, 1:1000), Rabbit polyclonal Anti-Stat1(10144-2-AP, 1:2000), Rabbit polyclonal Anti-p-Stat1(Tyr701) (28979-1-AP, 1:1000), Mouse monoclonal Anti-α-Tubulin (66031-1-Ig, 1:3000), Rabbit polyclonal Anti-FLAG (20543-1-AP, 1:5000) and Rabbit polyclonal Anti-HECTD1 (20605-1-AP, 1:500) were purchased from Proteintech; Rabbit polyclonal Anti-p-JAK1 (Tyr1034/1035) (3331S, 1:1000) and Rabbit monoclonal Anti-p-Stat6 (Tyr641) (56554S, 1:1000) were purchased from CST; Rabbit monoclonal Anti-FTH1 (A19544, 1:1000) and Rabbit Monoclonal Anti-NCOA4 (A25307, 1:500) was purchased from ABclonal; Rabbit monoclonal Anti-BRD4 (ab128874, 1:200) was purchased from Abcam; Mouse monoclonal Anti-BRD4 (67374-2-Ig, 1:2000) was purchased from Proteintech; Rabbit polyclonal Anti-DCAF16 (BD-PN3446, 1:500) was purchased from Biodragon; Mouse monoclonal Anti-β-actin (cat. No. TA-09, 1:1000), Alexa-594-conjugated Anti-rabbit IgG (ZF-0516, 1:2500), goat Anti-mouse HRP (ZDR5307, 1:2500) and goat Anti-rabbit HRP (ZDR5306, 1:2500) were purchased from ZSGB-Bio; Human recombinant protein IL4 (200-04) was purchased from Peprotech; Human recombinant protein IFNα 2a (P5646) was purchased from Beyotime.

Cell culture

Human HEK293T and HT1080 cells were purchased from Procell Life Science & Technology Co., Ltd (China). HEK293T cells were cultured in DMEM (Gibco) with 10% FBS (Life Technologies) and 100 units/ml penicillin and streptomycin, while HT1080 cells were cultured in MEM (Procell) with 10% FBS and 100 units/ml penicillin and streptomycin. Both cell lines were maintained at 37 °C in a 5% CO_2 humidified atmosphere. Prior to treatment, cells were grown to ~80% confluency and cultured in overnight serum-free medium. After treatment, cells were detached using 0.25% EDTA-trypsin, washed twice with prechilled PBS (Thermo Fisher Scientific, cat. no. C10010500), and collected by centrifugation at 500 g for 3 min. The cell pellets were snap-frozen in liquid nitrogen and stored at −80 °C until further use.

Compound treatment

For in vitro treatment, HEK293T cells were grown to 90% confluence, quickly rinsed with cold PBS, and harvested in 500 μL cold lysis buffer. Cell lysates from one 10 cm dish (~2 × 10⁷ cells) were incubated with 5 or 500 μM DPCC at 37 °C for 2 h, while DMSO was used as a vehicle control. The lysates were further incubated with 100 μM IPM (Kera-Fast, cat. no. EVU111) at room temperature (RT) for 1 h.

For in cellulo treatment, HEK293T cells were grown to 80% confluence, quickly rinsed with PBS, and treated with the indicated concentrations of DPCC. Cells were incubated in serum-free medium at 37 °C for the specific duration, then rinsed with PBS and harvested in cold lysis buffer. The lysates were further incubated with 100 μM IPM at RT for 1 h.

To analyze BRD4 expression following EtA-(S)-JQ1 treatment, HEK293T cells were grown to 80% confluence, and rinsed with PBS, and treated with EtA (5 μM), 11 (5 μM), 12 (5 μM), or EtA-(S)-JQ1 (5 μM) in serum-free medium at 37 °C for 4 h. Cells were rinsed with PBS and collected for subsequent experiments.

For analyzing the protein expression following DPCC treatment, HEK293T cells were grown to 80% confluence, rinsed with PBS, and treated with or without 20 μM DPCC in serum-free medium at 37 °C for 4 h. Cells were rinsed with PBS and collected for further analysis.

Preparation of cell lysates

Cells were lysed in pre-chilled HEPES buffer (50 mM HEPES, 150 mM NaCl, and 1% IGEPAL, pH 7.6) supplemented with 1× protease and

phosphatase inhibitors (Thermo Scientific, A32961) and 200 unit/mL catalase (Sigma-Aldrich, cat. no. C1345). After centrifugation at 18,000 g for 5 min at 4 °C, the supernatants were collected and incubated with 8 mM DTT at RT for 1 h to reduce reversibly oxidized cysteines. The lysates were then alkylated with 32 mM iodoacetamide at RT for 30 min in the dark with rotation. To quench the reactions and remove excess reagents, a methanol-chloroform system (aqueous phase/methanol/ chloroform, 4:4:1, v/v/v) was used. The precipitated proteins were collected by centrifugation at $1700 \times g$ for 20 min at 4 °C and washed twice with methanol/chloroform (1:1, v/v). Proteins were then re-pelleted by centrifugation at 16,000 g for 10 min at 4 °C. The resulting protein pellets were resuspended in 50 mM ammonium bicarbonate (NH_4HCO_3, Sigma-Aldrich, cat. no. A6141). Protein concentration was determined using a BCA assay (Tiangen, cat. no. PA115) and adjusted to 1 mg/mL.

Tryptic digestion

Each cell lysate sample (1 mg protein/mL in 1 mL volume) was digested with sequencing-grade trypsin (Sigma-Aldrich, cat. no. A6141) at a 1:50 enzyme-to-substrate ratio overnight at 37 °C. The resulting tryptic digests were desalted using HLB extraction cartridges (Waters, cat. no. 186000383) and then evaporated to dryness.

Capturing IPM-labeled peptides for QTRP

The desalted tryptic digests were resuspended in an aqueous solution containing 30% acetonitrile (MeCN). A CuAAC reaction was then carried out by adding 1 mM light or heavy Azido-UV-biotin, 10 mM sodium ascorbate, 1 mM TBTA, and 10 mM $CuSO_4$. After 2 h of incubation at RT under light protection, the reaction mixtures (the light and heavy isotopic tagged samples were combined in a ratio of 1:1 immediately following the reaction) were incubated with streptavidin beads for 2 h at RT. Streptavidin beads were washed twice with 50 mM NaOAc (sodium acetate, pH4.5), 50 mM NaOAc containing 2 M NaCl (sodium chloride, pH4.5), and deionized water, with vortexing and/or rotation to remove non-specific binding. The pelleted beads were resuspended in 25 mM ammonium bicarbonate, transferred to glass tubes (VWR), and irradiated with 365 nm UV light (Entela) for 2 h at RT with magnetic stirring. The supernatant was collected, dried under vacuum, and stored at −20 °C until LC MS/MS analysis.

Stable isotope dimethyl labeling

HEK293T cells were treated with the indicated drugs and controls, harvested, and processed into tryptic peptides. The resulting peptides were desalted using HLB extraction cartridges and evaporated to dryness as aforementioned. The desalted tryptic digests from both drug treatment groups and controls were reconstituted in 100 μL TEAB (100 mM) and incubated with CH_2O and CD_2O (4%, v/v, 12 μL), respectively, followed by the addition of $NaBH_3CN$ (0.6 M., 12 μL). After 1 h of incubation at room temperature, the reactions terminated by adding 48 μL 1% (v/v) ammonia solution (Aladdin) and 24 μL 5% formic acid (Sigma). The resulting light and heavy samples were mixed equally, desalted with HLB extraction cartridges, evaporated to dryness, and stored at −80 °C until LC-MS/MS analysis.

LC-MS/MS

For QTRP experiments, LC-MS/MS analyses were performed on a Q Exactive plus (Thermo Fisher Scientific) equipped with an Easy-nLC1000 system (Thermo Fisher Scientific) or a Q Exactive HF-X (Thermo Fisher Scientific) equipped with an UltiMate 3000 RSLC nano system (Thermo Fisher Scientific). Samples were reconstituted in 0.1 % formic acid followed by centrifugation (16,000 g for 10 min). For an Easy-nLC1000 system, the supernatants were pressure-loaded onto a 2 cm microcapillary precolumn packed with C18 (3 mm, 120 A˚, SunChrom, USA) and were then delivered onto a 12 cm 150-μm-inner diameter microcapillary analytical column packed with C18 (1.9 μm, 120 A˚, Dr. Maisch

GebH, Germany); peptides were separated using a linear gradient that consisted of 0 min, 7% B; 14 min, 10% B; 51 min, 20% B; 68 min, 30% B; 69–75 min, 95% B (A = water, 0.1% formic acid; B = MeCN, 0.1% formic acid) at a flow rate of 600 nL/min. For an UltiMate 3000 RSLC nano system, the supernatants were delivered onto a 1 cm self-packed trap column (150 μm inner diameter, 1.9 μm resin, ReproSilPur C18-AQ, Dr. Maisch GmbH). After loading and washing, peptides were transferred to a 15 cm column (150 μm inner-diameter, 1.9 μm resin, ReproSil-Pur C18-AQ, Dr. Maisch GmbH) and separated using a linear gradient that consisted of 0–10 min, 6% B from 10 to 15 min, 12–32% B from 15 to 70 min, 32–42% B from 70 to 80 min, 95% B from 80.1 to 85 min, and re-equilibration at 6% B from 85.1 to 88 min (A = water, 0.1% formic acid; B = MeCN, 0.1% formic acid) at a flow rate of 600 nL/min.

For a Q Exactive plus, the spray voltage was set to 2.0 kV and the heated capillary temperature to 320 °C in positive ion mode. The parameters used in full MS scans were as follows: scan range (m/z 300–1400), resolution (70,000), AGC target (3e6), and max injection time (20 ms). HCD MS/MS spectra were recorded in the data dependent mode using a Top 20 method. MS2 scans were acquired with scan range (m/z 100–1500), resolution (17,500), AGC target (1e6), and max injection time (60 ms). Fragmentation was performed in the higher energy collision dissociation (HCD) mode with normalized collision energy (NCE: 27), isolation window (m/z 1.6), dynamic exclusion (18 s), and charge exclusion (+1 or greater than +8).

For a Q Exactive HF-X, the ion source, electrospray ionization (ESI) was operated at a capillary voltage of 2.0 kV with ion transfer tube temperature 320 °C in positive ion mode. The parameters used in full MS scans were as follows: scan range (m/z 350–1550), resolution (120,000), AGC target (3e6), and max injection time (20 ms). HCD MS/MS spectra were recorded in the data dependent mode using a Top 25 method. MS2 scans were acquired with scan range (m/z 100-1500), resolution (15,000), AGC target (2e4), and max injection time (30 ms). Fragmentation was performed in the higher energy collision dissociation (HCD) mode with normalized collision energy (NCE: 27), isolation window (m/z 1.6), dynamic exclusion (15 s), and charge exclusion (+1 or greater than +8).

For stable isotope dimethyl labeling-based quantitative proteomics, LC-MS/MS analyses were performed on a Orbitrap Exploris 480 (Thermo Fisher Scientific) equipped with an Vanquish nano system (Thermo Fisher Scientific). Samples were reconstituted in 0.1 % formic acid followed by centrifugation (16,000 g for 10 min). The supernatants were pressure-loaded onto a 30 cm 100-μm-inner diameter microcapillary analytical column packed with C18 (1.9 μm, 120 A˚, Dr. Maisch GmbH, Germany); peptides were separated using a linear gradient that consisted of 0 min, 3% B; 3 min, 8% B; 115 min, 30% B; 120 min, 40% B; 122–150 min, 95% B (A = water, 0.1% formic acid; B = 80%ACN, 0.1% formic acid) at a flow rate of 300 nL/min. The spray voltage was set to 2.0 kV and the heated capillary temperature to 320 °C in positive ion mode. The parameters used in full MS scans were as follows: scan range (m/z 350-1500), resolution (60,000), AGC target (Custom), and max injection time (45 ms). HCD MS/MS spectra were recorded in the data dependent mode using a Top 20 method. MS2 scans were acquired with scan range (m/z 100–1500), resolution (15,000), AGC target (Custom), and max injection time (Custom). Fragmentation was performed in the higher energy collision dissociation (HCD) mode with normalized collision energy (NCE: 28), isolation window (m/z 1.6), dynamic exclusion (Custom), and charge exclusion (+1 or greater than +8).

Peptide identification and quantification

For peptide-level analysis, MS data was imported into the pFind studio v3.1.5 (http://pfind.org/software/pFind). Raw data files were searched against the *Homo sapiens* UniProt canonical (non-redundant) database. The precursor-ion mass tolerance was set to 10 ppm, and fragment ion mass tolerance to 20 ppm. A full-specific-tryptic search was

allowed with a maximum of three missed cleavages and a maximum of three modifications per peptide. For all analyzes, modifications of +15.9949 Da (methionine oxidation, M) and +57.0214 Da (iodoaceta-mide alkylation, C) were searched as variable modifications. For QTRP analysis, mass shifts of +252.12229 Da ($C_{11}H_{16}O_3N_4$) were also searched as variable modifications. An isotopic mass difference of 6.020132 Da ($^{12}C_6/^{13}C_6$) on PDMs was used for quantification. The FDRs at spectrum, peptide, and protein level were <1%. Quantitative analyses were per-formed using pQuant (embedded in the pFind studio)[63], which calcu-lates heavy to light ratios based on each identified MS scan with a 15 ppm-level m/z tolerance window, and assigns an interference score (Int. Score) ranging from zero to one. Lower Int. Scores indicate less coelution interference. The PSM-level quantification data from pQuant were collapsed into site-level quantification using in-house software with following filtering criteria: (i) PSMs with multiple probe-labeling cysteines were removed; (ii) PSMs with typically noisy peptides (i.e., missed cleavage, Met oxidation) were excluded; (iii) PSM quantifica-tion ratios (e.g., different charge states) from the same probe-labeled site were grouped to calculate median values and standard deviations, resulting in site-level quantification matrices; (iv) if the medium $R_{H/L}$ values ≤4, site-level quantification ratios with an Int. Score higher than 0.5 were excluded. High values obtained from unpaired peaks (i.e., detected in only one channel or only in untreated samples, or 'sin-gletons') were kept, as their Int. Score was defined as 1.0 by default in pQuant. Site-level quantification results for each QTRP experiment were provided along with the corresponding RAW data, accessible via the iProX (identifier PXD044946). Only site-level quantification ratios with a coefficient of variation (CV) below 40% were used for further data analysis and graphic illustration. Sites with $R_{H/L}$ values ≥ 4 (i.e., ≥75% reductions in probe labeling) were considered as engaged cysteines, while those 'singletons' were marked in the data matrices. For in cellulo QTRP analysis, site-level quantification ratios from six replicates were normalized with protein abundance changes deter-mined by stable isotope dimethyl labeling-based quantitative pro-teomics and subjected to statistical evaluation based on the LIMMA-test. Cysteines with a normalized ratio of R ≥ 2 and significantly dif-ferent intensities (p-value < 0.05) in light and heavy channels were considered high-confidence target candidates.

For stable isotope dimethyl labeling-based quantitative proteomics, MS data was processed by the FragPipe v22.0 (https://github.com/Nesvilab/FragPipe/releases) with MSFragger 4.1 and IonQuant 1.10.27 search engines using default settings[64]. Raw data files were sear-ched against the Homo sapiens UniProt canonical database. Precursor and fragment mass tolerance were set to 20 ppm. A specific-tryptic search was allowed with a maximum of two missed cleavages. Light dimethylation (+28.0313 Da, C_2H_4), heavy demethylation (34.0631 Da, $^{13}C_2D_4$), and methionine oxidation (+15.9949 Da, M) were searched as variable modifications, and iodoacetamide alkylation (+57.0214 Da, C) was searched as a fixed modification. A maximum of three modifications were allowed per peptide. MS1-based quantification was performed by IonQuant (embedded in FragPipe), resulting in "ptm.tsv" data matrices for further analysis. The LIMMA-test was used to generate adjusted p-values, which were plotted against the average fold-change of each protein to create volcano plots. Proteins with a $\log_2$(fold change) >1 and adjusted p value < 0.01 were considered significantly changed.

DrugBank analysis
Engaged proteins were queried against the DrugBank database (Ver-sion 5.1)[65] and classified into DrugBank and non-DrugBank proteins.

Functional annotation of engaged cysteines
Functional annotation of engaged cysteines was performed using an in-house Python script against the UniProtKB/Swiss-Prot Protein Knowledge database (release-2020_10). Relevant Uniprot entries were text-mined for available functional annotations at the residue level,

focusing on enzyme catalytic residues (active sites), disulfide bonds, DNA binding sites and modified sites.

CorrSite2.0
CorrSite was used to identify potential allosteric ligand binding sites based on motion correlation analysis between allosteric and orthos-teric cavities. The 3D structure of JAK1 (PDB#: 6TPE) was used as input, with the A chain of JAK1 selected for the cavity detection. Eleven potential cavities were detected on the surface of JAK1, with cavity_1 chosen as the orthosteric pocket. Sites with a Zscore>0.5 were con-sidered allosteric sites. Based on this criterion, six potential allosteric sites were discovered: Cavity_7 (1.77), Cavity_4 (1.3), Cavity_2 (1.0), Cavity_10 (0.89), Cavity_3 (0.86), Cavity_6 (0.56). Notably, C988 of JAK1 was located within Cavity_10.

Expression of epitope-tagged proteins
pcDNA3.1-3xFlag-*JAK1* (NM_002227), pcDNA3.1-3xFlag-*NCOA4* (F102297), pcDNA3.1-3xFlag-*HECTD1*(NM_015382) and pcDNA3.1-3xFlag-*HECTD1-C1368S* were purchased from YouBao (China). The point mutation plasmid was generated using the Fast Mutagenesis System (TransGen Biotech, cat. No. FM111-02) with the following pri-mers. The primers were synthesized by Tsingke Biotechnology and the mutation sequences were confirmed by DNA sequencing.

Gene	Primer-F	Primer-R
JAK1-C988S	ATGCCGTTCAGATTTCTAAGGGGATG	GAAATCTGAACGGCAT ATTTTTAGCTGCTG
NCOA4-C244S	CAGACTTCTTCCAGAGCCAGCAATTTCTTC AATAATG	CATTATTGAAGAAATT GCTGGCTCTGGAAGA AGTCTG
HECTD1-C1368S	TCTTGTCTGGAGAGTTGTTTTTCACCA AGCTGCT	AAACAACTCTCCAGACA AGACATCTGCTGCTG

For both wild-type and corresponding mutants, transfection was carried out by incubating 5 μg of each of plasmids and 10 μL of ExFect Transfection Reagent (Vazyme, cat. No. T101-01) into 50%-confluent HEK293T cells on a 6-well plate, or 20 μg of each of plasmids and 40 μL of ExFect Transfection Reagent into 50%-confluent HEK293T cells on a 10 cm dish. Cells were cultured in DMEM supplemented with 10% FBS for 48 h, then collected for subsequent experiments.

siRNA knockdown of target gene
HEK293T cells were seeded in a 6-well plate at a density of 5,000 cells/well and cultured overnight. The cells were then transfected with 20 nM target siRNA (synthesized by GenePharma) or scrambled siRNA using 7.5 μL Lipofectamine RNAiMAX Transfection Reagent (Invitro-gen), and incubated in Opti-MEM Reduced Serum Medium (Invitro-gen) for 48 h. After transfection, cells were harvested for immunoblotting. The target siRNA sequences are as follows:

HECTD1 siRNA#1	AGAUAAAGGUGGUGAUAUA
HECTD1 siRNA#2	GAGAACACUUGGAGAGAUU
NCOA4 siRNA#1	ACAAAGAUCUAGCCAAUCA
NCOA4 siRNA#2	GACCUUAUUUAUCAGCUUA
DCAF16 siRNA#1	CCTCAGTAACCTACTGCCAGCTGAA
DCAF16 siRNA#2	CCTTTAAATCCTAATTCCTGGTTGT

Natamycin-alkyne labeling
HEK293T cells were treated with either DMSO or 20 μM natamycin alkyne probe for 4 h. For the competition experiment, cells were pre-

incubated with 20 μM natamycin at 37 °C for 2 h, followed by treatment with 20 μM natamycin alkyne probe at 37 °C for 4 h. After treatment, cells were rinsed with PBS and lysed by sonication to prepare western blotting samples. Total protein concentration was determined by a BCA assay, and samples were normalized to a total volume of 150 μL (1 mg/mL), with 30 μL used as input. To carry out the CuAAC reaction, 120 μL of lysate was mixed with 3 μL of click reaction mix (containing 2.5 μL 40 mM N_3-Biotin solution, 5 μL 100 mM sodium ascorbate, 1 μL 50 mM TBTA solution in DMSO and 5 μL 100 mM $CuSO_4$). The mixture was incubated for 2 h at RT with gentle agitation. Following incubation, 20 μL of pre-washed streptavidin agarose bead slurry was added, and the samples were incubated overnight at RT with gentle agitation. Afterward, the supernatant was aspirated by centrifugation at 1700 g for 3 min at RT. The beads were washed 3× with lysis buffer. For elution, beads were boiled for 5 min in 30 μL 1× loading buffer, and the eluates were collected by centrifugation. The samples were then analyzed by immunoblotting.

Immunoprecipitation for analyzing the drug-target interactions

HEK293T cells expressing flag-tagged wild-type and its corresponding mutant were treated with each drug at the indicated concentrations for 4 h. After treatment, the cells were washed with PBS and lysed. The lysates were then labeled with BIAM (100 μM) for 1 h for RT. Flag-tagged wild-type and mutant proteins were immunoprecipitated from 1 mg of lysate using 20 μL of streptavidin sepharose (GE, 17-5113-01). The samples were incubated at 4 °C with rotation for 16 h, allowing for binding to the beads. After incubation, the agarose resin was collected and washed with lysis buffer. Th proteins were eluted using 1× loading buffer and analyzed by immunoblotting.

Immunoprecipitation for the interaction between NCOA4 and FTH1

HEK293T cells expressing flag-tagged wild-type and its mutant C244S were treated with drugs at the indicated concentrations for 4 h. After treatment, the cells were washed with PBS and lysed. Flag-tagged wild-type and mutant were immunoprecipitated from 1 mg of lysate using 20 μL of anti-Flag M2 affinity gel (Sigma-Aldrich, A2220) by rotation. The samples were incubated at 4 °C for 16 h. After incubation, the agarose resin was collected, washed with lysis buffer, and the proteins were eluted with 1× loading buffer. The eluates were analyzed by immunoblotting to detect the proteins of interest.

Western blotting

Equal amounts of protein samples (20 μg) were mixed with 5×loading buffer (250 mM Tris-HCl, pH 6.8, 10% SDS, 0.5% bromophenol blue, 50% glycerin and 200 mM DTT), boiled for 5 min, and separated on 10% SDS-PAGE gels. After electrophoresis, proteins were transferred to a PVDF membrane (0.45 μm, Millipore, U.S.), and blocked with 5% milk or BSA (for phosphorylation detection) in TBST for 1 h at RT. The membrane was then washed three times with TBST (5 min each time) and probed with the indicated primary antibody at 4 °C overnight. Following incubation, the membrane was washed three times with TBST, and then incubated with the HRP-conjugated secondary antibodies for 2 h at RT. The immunoblots were detected using ECL chemiluminescence (CWBIO, cat. No. CW0049S) following the manufacturer's protocol, and visualized on a Tanon 5200 scanner (Shanghai, China).

Quantification of gel bands by an image J

Raw TIFF files were opened on ImageJ[66]. The background of image was subtracted, and then the image was inverted. The bands were selected using a rectangular tool, and the integrated density of the selected lanes was measured. The integrated density of the target protein was corrected by dividing by the integrated density of the internal reference protein. Unpaired student's t-test was performed to generate a p-value for comparisons between control and treatment groups.

Real-time PCR

Total RNA was isolated using RNAiso plus (Takara) according to the manufacturer's protocol. One microgram of total RNA was used for cDNA synthesis using the PrimeScript™ RT Master Mix (Takara, RR036A), following the manufacturer's protocol. The resulting cDNA was used amplifying specific target genes via SYBR Green Real-time PCR Master Mix (TOYOBO, QKD-201). Data were normalized to the internal control GAPDH. Relative gene expression levels were calculated using the delta Ct (2 − ΔΔCt) method. The sequences of primers (synthesized by Tsingke Biotechnology) used for qPCR are:

Gene	Primer-F	Primer-R
GAPDH	GAAGGTGAAGGTCGGAGTC	GAAGATGGTGATGGGATTTC
PTGS2	CTGCGCCTTTTCAAGGATGG	GGGGATACACCTCTCCACCA
FTH1	GCCGAGAAACTGATGAAGCTGC	GCACACTCCATTGCATTCAGCC
BRD4	ACCTCCAACCCTAACAAGCC	TTTCCATAGTGTCTTGAGCACC

Immunofluorescence

Fluorescence was observed with a laser scanning microscope (ZEISS, LSM880 ELYRAS). For the analysis of BRD4, HEK293T cells were seeded into confocal dishes and grown overnight. Cells were treated with or without drugs at the indicated concentrations. After a 4 h incubation at 37 °C, cells were washed with PBS and fixed in paraformaldehyde for 30 min at RT. The cells were then permeabilized with 0.2 % Triton X-100 for 30 min at 4 °C and blocked in 3 % BSA in PBS. Fixed cells were incubated with the corresponding primary antibody at 4 °C overnight, followed by incubation with the appropriate fluorescent secondary antibodies. The nuclei were stained with DAPI (ZSGB, ZLI-9557, diluted at 1:1000). For intracellular Fe^{2+} detection, HT1080 cells were seeded into confocal dishes and grown overnight. The cells were treated with DMSO, parthenolide (20 μM), or Deferoxamine mesylate (50 μM) as a positive control for 4 h at 37 °C. The cells were then co-stained with FerroOrange (1 μM) and Hoechst 33342 (1 μg/mL) in serum-free DMEM medium for 30 min at 37 °C, followed by washing with PBS. For lipid ROS detection, HEK293T cells in complete DMEM (containing 10% vol/vol FBS) were seeded into 6-well plate. Cells expressing wild-type NCOA4 or NCOA4 C244S mutant were grown to ~50% confluency and cultured in DMEM supplemented with 10% FBS for another 24 h. The cells were then seeded into confocal dishes and grown overnight. After treatment with or without parthenolide (20 μM) for 4 h, the cells were co-stained with BODIPY-C11 dye (5 μM) and Hoechst 33342 (1 μg/mL). For each condition, three representative images were taken. Quantification of fluorescence intensity was performed using ImageJ software. Statistical analysis was performed using unpaired Student's t-test to generate p-values between control and treatment groups.

Flow cytometry for ROS assays

HT1080 cells were seeded and treated with indicated drugs at 20 μM or controls for 4 h at 37 °C. Following incubation, cells were washed with PBS and stained with 10 μM dihydroethidium (DHE) (Solarbio®-Life Sciences) for 30 min. The cells were then harvested and analyzed by BD LSRFortessa SORP (BD Science, New Jersey, USA). We use FSC (forward scatter) and SSC (side scatter) for gating to find viable, single cell events. De-adhesion was used after FSC/SSC using FSC-A/FSC-H. Following gating, 10,000 single cell events were collected. Cellular ROS level (mCherry-A) was examined and analyzed to produce a bivariate scatter diagram. The data obtained was analyzed using FlowJo_v10.8.1 software.

In vitro kinase assay

The JAK1 kinase activity was assessed using the ADP-Glo™ Kinase Assay Kit following the manufacturer's protocol. The reaction was performed in 1× reaction buffer (supplemented with 50 μM ATP and 50 μM DTT)

containing JAK1 kinase (30 ng). The drug being tested (either Natamycin or Tofacitinib) was added to the reaction mixture at the specified concentrations. After incubation at RT for 1 h, the ADP-Glo™ reagent was added to the reaction mixture and incubated at RT for 40 min. Subsequently, the kinase detection reagent was added, and the mixture was incubated at RT for an additional 1 h. The luminescence of the samples was measured using a Luminescence detection system (Promega), with an integration time of 1 s.

In vitro peptide phosphorylation assay

The JAK1 kinase activity was also assessed using the PhosphoSens® Protein Kinase Assay (AssayQuant Technologies Inc.), employing the optimized JAK1 AQT0663B peptide as the substrate. The reaction mixture contained 10 μM AQT0663B peptide substrate, 1 mM ATP, and 1 mM DTT in a reaction buffer. The reaction was initiated by adding 80 nM of JAK1 kinase, which was pre-incubated with or without the indicated compounds. The JAK1-catalyzed phosphorylation of the peptide substrate was monitored continuously at 30 °C using a plate reader. The excitation and emission wavelengths were set at 360 nm and 485 nm, respectively. The time traces were corrected by subtracting the "none JAK1" control. The initial reaction rates were calculated from the slope of the linear portion of the fluorescence intensity curve.

MTT assay

HEK293T cells (~ 2500 cells) were plated in each well of a 96-well plate and incubated with 100 μL DMEM supplemented with 10% FBS. Drug was added to each well at final concentrations ranging from 1 to 20 μM, using from 5 mM stock solutions dissolved in DMSO. The cells were incubated at 37 °C, 5% CO_2 for 24 h. After the incubation, 20 μL of MTT (3-(4,5-dimethylthiazol-2-yl)-2,5-diphenyltetrazolium bromide, 5 mg/mL) was added to each well. The cells were incubated at 37 °C for an additional 4 hours, during which the MTT reagent was metabolized by living cells to produce a purple formazan product. After incubation, 150 μL of DMSO was added to dissolve the formazan, followed by vortexing for 10 minutes at room temperature. The absorbance was measured at 490 nm using a microplate reader. The experiments were performed in five biological replicates.

Statistical analysis

The experiments were not randomized, and the investigators were not blinded to allocation during experiments or outcome assessment. No statistical methods were used to predetermine sample size. Statistical analyses were performed using GraphPad Prism (v.7.0 and v.8.0).

Reporting summary

Further information on research design is available in the Nature Portfolio Reporting Summary linked to this article.

Data availability

The mass spectrometry proteomics data generated in this study have been deposited to the ProteomeXchange Consortium (http://proteomecentral.proteomexchange.org) via the iProX partner repository[67] with the dataset identifier PXD044946. Source data are provided with this paper.

Code availability

In house algorithms for data processing and functional annotation developed in our lab are available on our GitHub repository site (https://github.com/morpheusliu/Post-processing-program-for-pFind3-results). The code is also available on Zenodo (https://doi.org/10.5281/zenodo.15291291).

References

1. Boike, L., Henning, N. J. & Nomura, D. K. Advances in covalent drug discovery. *Nat. Rev. Drug Discov.* **21**, 881–898 (2022).
2. Kornberg, M. D. et al. Dimethyl fumarate targets GAPDH and aerobic glycolysis to modulate immunity. *Science* **360**, 449–453 (2018).
3. Humphries, F. et al. Succination inactivates gasdermin D and blocks pyroptosis. *Science* **369**, 1633–1637 (2020).
4. Andersen, J. L. et al. Dimethyl fumarate is an allosteric covalent inhibitor of the p90 ribosomal S6 kinases. *Nat. Commun.* **9**, 4344 (2018).
5. Blewett, M. M. et al. Chemical proteomic map of dimethyl fumarate-sensitive cysteines in primary human T cells. *Sci. Signal.* **9**, rs10 (2016).
6. Zaro, B. W. et al. Dimethyl fumarate disrupts human innate immune signaling by targeting the IRAK4-MyD88 complex. *J. Immunol.* **202**, 2737–2746 (2019).
7. Wang, C., Weerapana, E., Blewett, M. M. & Cravatt, B. F. A chemoproteomic platform to quantitatively map targets of lipid-derived electrophiles. *Nat. Methods* **11**, 79–85 (2014).
8. Maurais, A. J. & Weerapana, E. Reactive-cysteine profiling for drug discovery. *Curr. Opin. Chem. Biol.* **50**, 29–36 (2019).
9. Backus, K. M. et al. Proteome-wide covalent ligand discovery in native biological systems. *Nature* **534**, 570–574 (2016).
10. Vinogradova, E. V. et al. An activity-guided map of electrophile-cysteine interactions in primary human T cells. *Cell* **182**, 1009–1026.e1029 (2020).
11. Zanon, P. R. A., Lewald, L. & Hacker, S. M. Isotopically labeled desthiobiotin azide (isoDTB) tags enable global profiling of the bacterial cysteinome. *Angew. Chem.* **59**, 2829–2836 (2020).
12. Spradlin, J. N., Zhang, E. & Nomura, D. K. Reimagining druggability using chemoproteomic platforms. *Acc. Chem. Res.* **54**, 1801–1813 (2021).
13. Chung, C. Y. et al. Covalent targeting of the vacuolar H(+)-ATPase activates autophagy via mTORC1 inhibition. *Nat. Chem. Biol.* **15**, 776–785 (2019).
14. Henning, N. J. et al. Deubiquitinase-targeting chimeras for targeted protein stabilization. *Nat. Chem. Biol.* **18**, 412–421 (2022).
15. Fu, L. et al. A quantitative thiol reactivity profiling platform to analyze redox and electrophile reactive cysteine proteomes. *Nat. Protoc.* **15**, 2891–2919 (2020).
16. Tian, C. et al. Multiplexed thiol reactivity profiling for target discovery of electrophilic natural products. *Cell Chem. Biol.* **24**, 1416–1427.e1415 (2017).
17. Wang, W. et al. An arabidopsis secondary metabolite directly targets expression of the bacterial type III secretion system to inhibit bacterial virulence. *Cell Host Microbe* **27**, 601–613.e607 (2020).
18. Wang, M. R. et al. Identification of NLRP3 as a covalent target of 1,6-O,O-diacetylbritannilactone against neuroinflammation by quantitative thiol reactivity profiling (QTRP). *Bioorg. Chem.* **119**, 105536 (2022).
19. Liu, X. et al. Discovery of CAPE derivatives as dual EGFR and CSK inhibitors with anticancer activity in a murine model of hepatocellular carcinoma. *Bioorg. Chem.* **107**, 104536 (2021).
20. Ábrányi-Balogh, P. & Keserű, G. M. in *Advances in Chemical Proteomics* 47–73 (Elsevier, 2022).
21. Lipinski, C. A. Lead-and drug-like compounds: the rule-of-five revolution. *Drug Discov. Today* **1**, 337–341 (2004).
22. Kuljanin, M. et al. Reimagining high-throughput profiling of reactive cysteines for cell-based screening of large electrophile libraries. *Nat. Biotechnol.* **39**, 630–641 (2021).
23. Boatner, L. M., Palafox, M. F., Schweppe, D. K. & Backus, K. M. CysDB: a human cysteine database based on experimental quantitative chemoproteomics. *Cell Chem. Biol.* **30**, 683–698.e683 (2023).
24. White, M. E. H., Gil, J. & Tate, E. W. Proteome-wide structural analysis identifies warhead- and coverage-specific biases in cysteine-focused chemoproteomics. *Cell Chem. Biol.* **30**, 828–838.e824 (2023).

25. Tsherniak, A. et al. Defining a cancer dependency map. *Cell* **170**, 564–576.e516 (2017).

26. Murray, P. J. The JAK-STAT signaling pathway: input and output integration. *J. Immunol.* **178**, 2623–2629 (2007).

27. Patel, B. K. et al. Stat6 and Jak1 are common elements in platelet-derived growth factor and interleukin-4 signal transduction pathways in NIH 3T3 fibroblasts. *J. Biol. Chem.* **271**, 22175–22182 (1996).

28. Quambusch, L. et al. Covalent-allosteric inhibitors to achieve akt isoform-selectivity. *Angew. Chem.* **58**, 18823–18829 (2019).

29. Wrobleski, S. T. et al. Highly selective inhibition of tyrosine kinase 2 (TYK2) for the treatment of autoimmune diseases: discovery of the allosteric inhibitor BMS-986165. *J. Med. Chem.* **62**, 8973–8995 (2019).

30. Kemper, E. K., Zhang, Y., Dix, M. M. & Cravatt, B. F. Global profiling of phosphorylation-dependent changes in cysteine reactivity. *Nat. Methods* **19**, 341–352 (2022).

31. Abegg, D. et al. Chemoproteomic profiling by cysteine fluoroalkylation reveals myrocin g as an inhibitor of the nonhomologous end joining DNA repair pathway. *J. Am. Chem. Soc.* **143**, 20332–20342 (2021).

32. Koo, T. Y., Lai, H., Nomura, D. K. & Chung, C. Y. N-Acryloylindole-alkyne (NAIA) enables imaging and profiling new ligandable cysteines and oxidized thiols by chemoproteomics. *Nat. Commun.* **14**, 3564 (2023).

33. Yang, F., Jia, G., Guo, J., Liu, Y. & Wang, C. Quantitative chemoproteomic profiling with data-independent acquisition-based mass spectrometry. *J. Am. Chem. Soc.* **144**, 901–911 (2022).

34. Xie, J., Wang, S., Xu, Y., Deng, M. & Lai, L. Uncovering the dominant motion modes of allosteric regulation improves allosteric site prediction. *J. Chem. Inf. Model.* **62**, 187–195 (2022).

35. Kavanagh, M. E. et al. Selective inhibitors of JAK1 targeting an isoform-restricted allosteric cysteine. *Nat. Chem. Biol.* **18**, 1388–1398 (2022).

36. Dowdle, W. E. et al. Selective VPS34 inhibitor blocks autophagy and uncovers a role for NCOA4 in ferritin degradation and iron homeostasis in vivo. *Nat. cell Biol.* **16**, 1069–1079 (2014).

37. Mancias, J. D. et al. Ferritinophagy via NCOA4 is required for erythropoiesis and is regulated by iron dependent HERC2-mediated proteolysis. *eLife* **4**, e10308 (2015).

38. Zhou, H. et al. NCOA4-mediated ferritinophagy is involved in ionizing radiation-induced ferroptosis of intestinal epithelial cells. *Redox Biol.* **55**, 102413 (2022).

39. Fang, X. et al. Ferroptosis as a target for protection against cardiomyopathy. *Proc. Natl. Acad. Sci. USA* **116**, 2672–2680 (2019).

40. Stockwell, B. R. Ferroptosis turns 10: Emerging mechanisms, physiological functions, and therapeutic applications. *Cell* **185**, 2401–2421 (2022).

41. Chamberlain, P. P. & Hamann, L. G. Development of targeted protein degradation therapeutics. *Nat. Chem. Biol.* **15**, 937–944 (2019).

42. Schapira, M., Calabrese, M. F., Bullock, A. N. & Crews, C. M. Targeted protein degradation: expanding the toolbox. *Nat. Rev. Drug Discov.* **18**, 949–963 (2019).

43. Zhang, X., Crowley, V. M., Wucherpfennig, T. G., Dix, M. M. & Cravatt, B. F. Electrophilic PROTACs that degrade nuclear proteins by engaging DCAF16. *Nat. Chem. Biol.* **15**, 737–746 (2019).

44. Henning, N. J. et al. Discovery of a covalent FEM1B recruiter for targeted protein degradation applications. *J. Am. Chem. Soc.* **144**, 701–708 (2022).

45. Spradlin, J. N. et al. Harnessing the anti-cancer natural product nimbolide for targeted protein degradation. *Nat. Chem. Biol.* **15**, 747–755 (2019).

46. Pei, J. et al. Piperlongumine conjugates induce targeted protein degradation. *Cell Chem. Biol.* **30**, 203–213.e217 (2023).

47. Molnar, J. & Somberg, J. C. The clinical pharmacology of ethacrynic acid. *Am. J. Ther.* **16**, 86–92 (2009).

48. Zengerle, M., Chan, K. H. & Ciulli, A. Selective small molecule induced degradation of the BET bromodomain protein BRD4. *ACS Chem. Biol.* **10**, 1770–1777 (2015).

49. Andrieu, G. P. & Denis, G. V. BET proteins exhibit transcriptional and functional opposition in the epithelial-to-mesenchymal transition. *Mol. Cancer Res. MCR* **16**, 580–586 (2018).

50. Lv, K. et al. HectD1 controls hematopoietic stem cell regeneration by coordinating ribosome assembly and protein synthesis. *Cell Stem Cell* **28**, 1275–1290 e1279 (2021).

51. Sarkar, A. A. & Zohn, I. E. Hectd1 regulates intracellular localization and secretion of Hsp90 to control cellular behavior of the cranial mesenchyme. *J. Cell Biol.* **196**, 789–800 (2012).

52. Tunyasuvunakool, K. et al. Highly accurate protein structure prediction for the human proteome. *Nature* **596**, 590–596 (2021).

53. Lim, M. et al. DCAF16-Based covalent handle for the rational design of monovalent degraders. *ACS Cent. Sci.* **17**, 1318–1331 (2024).

54. Cui, Z. et al. Ethacrynic acid targets GSTM1 to ameliorate obesity by promoting browning of white adipocytes. *Protein cell* **12**, 493–501 (2021).

55. Ye, Z. et al. Chemoproteomic profiling reveals ethacrynic acid targets adenine nucleotide translocases to impair mitochondrial function. *Mol. Pharm.* **15**, 2413–2422 (2018).

56. Li, H. et al. Assigning functionality to cysteines by base editing of cancer dependency genes. *Nat. Chem. Biol.* **19**, 1320–1330 (2023).

57. Palafox, M. F., Desai, H. S., Arboleda, V. A. & Backus, K. M. From chemoproteomic-detected amino acids to genomic coordinates: insights into precise multi-omic data integration. *Mol. Syst. Biol.* **17**, e9840 (2021).

58. Klaeger, S. et al. The target landscape of clinical kinase drugs. *Science* **358**, eaan4368 (2017).

59. Lechner, S. et al. Target deconvolution of HDAC pharmacopoeia reveals MBLAC2 as common off-target. *Nat. Chem. Biol.* **18**, 812–820 (2022).

60. King, E. A. et al. Chemoproteomics-enabled discovery of a covalent molecular glue degrader targeting NF-kappaB. *Cell Chem. Biol.* **30**, 394–402.e9 (2023).

61. Fang, Y. et al. Inhibiting ferroptosis through disrupting the NCOA4-FTH1 Interaction: a new mechanism of action. *ACS Cent. Sci.* **7**, 980–989 (2021).

62. Meyer, M. J. et al. Interactome INSIDER: a structural interactome browser for genomic studies. *Nat. Methods* **15**, 107–114 (2018).

63. Chi, H. et al. Comprehensive identification of peptides in tandem mass spectra using an efficient open search engine. *Nat. Biotechnol.* **36**, 1059–1061 (2018).

64. Kong, A. T., Leprevost, F. V., Avtonomov, D. M., Mellacheruvu, D. & Nesvizhskii, A. I. MSFragger: ultrafast and comprehensive peptide identification in mass spectrometry–based proteomics. *Nat. Methods* **14**, 513–520 (2017).

65. Wishart, D. S. et al. DrugBank: a knowledgebase for drugs, drug actions and drug targets. *Nucleic Acids Res.* **36**, D901–D906 (2008).

66. Schindelin, J. et al. Fiji: an open-source platform for biological-image analysis. *Nat. Methods* **9**, 676–682 (2012).

67. Ma, J. et al. iProX: an integrated proteome resource. *Nucleic Acids Res.* **47**, D1211–D1217 (2019).

Acknowledgements

Author contributions

C.T. performed most experiments and analyzed the data. L.S. performed chemical synthesis. K.L. and L.F. performed experiments and/or analyzed the data. Y.Z. analyzed the data. W.C. performed LC-MS/MS

Competing interests

The authors declare no competing interests.

Additional information

Supplementary information The online version contains supplementary material available at https://doi.org/10.1038/s41467-025-60068-x.

Correspondence and requests for materials should be addressed to Fuchu He or Jing Yang.

Peer review information *Nature Communications* thanks the anonymous reviewer(s) for their contribution to the peer review of this work. A peer review file is available.

Reprints and permissions information is available at http://www.nature.com/reprints

Publisher's note Springer Nature remains neutral with regard to jurisdictional claims in published maps and institutional affiliations.